DIFFUSION IMAGING OF LIPID MEMBRANES: DEVELOPING MULTI-PULSE NMR TO IMAGE STATIC MEMBRANE SAMPLES

by

Kevin Thomas Bivona

Bachelor of Science, University of Tennessee at Chattanooga, 2009

submitted to the graduate faculty of

Dietrich School of Arts and Sciences, Department of Chemistry in partial fulfillment

of the requirements for the degree of Master of Science

University of Pittsburgh

2012

UNIVERSITY OF PITTSBURGH

Dietrich School of Arts and Sciences

this thesis was presented

by

Kevin Thomas Bivona

It was defended on

March 30, 2012

and approved by

Dr. Steve Weber, Professor, Department of Chemistry

Dr. Renã Robinson, Assistant Professor, Department of Chemistry

Thesis Advisor: Dr. Megan M. Spence, Assistant Professor, Department of Chemistry

DIFFUSION IMAGING OF LIPID MEMBRANES:
DEVELOPING MULTI-PULSE NMR TO IMAGE STATIC MEMBRANE SAMPLES

Kevin Bivona, MS

University of Pittsburgh, 2012

ABSTRACT

A multi-pulse (MP), pulsed-field gradient (PG) stimulated echo (STE) nuclear magnetic resonance (NMR) pulse program was constructed and refined using ethylene glycol (EG), with the goal of providing a detailed diffusion image of a lipid membrane. This MP PGSTE NMR technique offers a useful combination of magnetic resonance imaging (MRI) and NMR tools that may provide images of lipid rafts at a length scale that is not restricted by the diffraction limit. MP NMR was used to provide homonuclear dipole-dipole decoupling, directly replacing magic-angle spinning (MAS), in a PGSTE NMR pulse program. Optimizing the use of MP NMR for EG and lipids, it was found that moving the carrier frequency ~2.5 kHz off resonance and shortening the cycle time to the minimum allowed by the probe hardware (in this case 43.2 μs at a power level of 139 kHz) produced the best results. By eliminating the use of magic-angle spinning (MAS), the gradient coils in the NMR diffusion-imaging probe may be placed closer to the sample, increasing their effect. Future work is needed to apply MP PGSTE NMR to static lipid samples. A basic PGSTE NMR diffusion measuring pulse program was used to determine the self-diffusion coefficient, D, of EG with the results showing D_{self} for EG was 6.5×10^{-11} m^2s^{-1}.

Table of Contents

List of Figures

I. INTRODUCTION & BACKGROUND INFORMATION

Producing a nanoscale spatial image of an intact cellular membrane has the potential to bring a better understanding of intracellular processes, such as pathology and viral entry into a cell. The goal of the work presented here is to combine techniques from magnetic resonance imaging (MRI) and nuclear magnetic resonance (NMR) spectroscopy to produce a nanoscale image of a lipid membrane. This goal will be met through the use of multi-pulse (MP) and pulsed-field gradient (PG) stimulated echo (STE) NMR for diffusion imaging, applied to static model lipid-membrane samples. Previously, work was done toward achieving this goal, but the technological requirements limited the practical application of the MP NMR with gradients.[1] In the decades since that work, electronic hardware has advanced significantly, and hence, the techniques have been revisited. Recent work by Dvinskikh and Furó has shown the viability of combining MP and PGSTE NMR,[2] and expanding on this work, we have applied the technique to membrane systems in lipid vesicles.

The work presented here explores model membrane systems in search of evidence related to lipid raft theory.[3] New models of the cell membrane have evolved in which the membrane is a heterogeneous mixture of lipids, proteins, and cholesterol. The diversity of lipids present in a cellular membrane, as well as the presence of cholesterol, results in multiple phases within the membrane.[3] The result is the formation of well-organized lipid domains that separate different types of lipids while sequestering certain transmembrane proteins. According to lipid raft theory, lipids, as well as proteins, play important roles in transmembrane processes; biophysical processes, from signaling to viral entry into the cell, are thought to be controlled by the membrane proteins as well as lipids.[5, 6] The membrane lipids in this model play a role in determining the location of transmembrane proteins, and experimental evidence has shown that cholesterol is important in the organization of membrane lipids and proteins into ordered domains.[4-6] The illustration in Figure 1 shows a schematic of a cell membrane that contains a

lipid domain. In Figure 1, the white lipids shown forming a domain have a higher affinity for the transmembrane proteins than the red lipids, resulting in the protein's sequestration. The black arrow indicates the confined diffusion of the lipids within the domain.

Proteins are known to have an active role in viral entry into a cell; *e.g.* CD4 is theorized to reside in lipid rafts on T-cells. It interacts with gp120 and gp41 of the HIV pathogen, allowing it to infect a host cell by hijacking a lipid raft.[6, 7] After taking control of a lipid domain in the membrane, HIV will exploit the cell's resources in order to carry out its infection process.[6] Because many membrane proteins are sequestered within lipid rafts, it is the segregation of protein-associating lipids that will influence the mechanism pathogens use to gain access into a cell.[6] Therefore, paramount to understanding the means by which various pathogens evade responses from the immune system is the study of membrane organization and the presence of lipid domains.

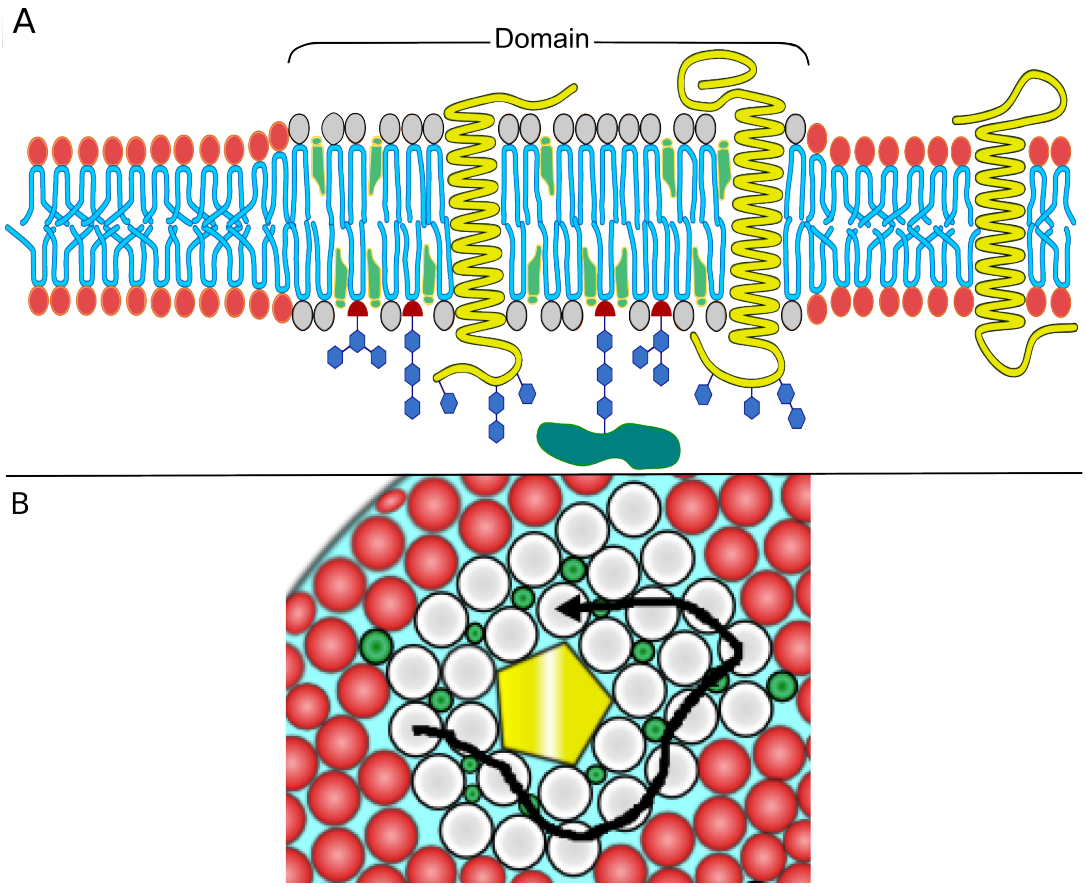

Figure 1: Structure of Lipid Domain. The cartoons show a lipid raft in a membrane; a side-on view is presented in part A, and a top-down view is presented in part B. Domain components are generally lipids (their head groups are represented as red and white objects, hydrophobic tails are shown in light blue, and functionalized parts are dark blue), cholesterol (green), proteins (yellow). The black arrow indicates a confined diffusion path of a lipid traversing through the domain.

A. ANISOTROPIC INTERACTIONS IN NMR

A lipid bilayer (Figure 1) is a liquid-crystalline system, and it will show anisotropic features when studied via NMR. These spectral features can provide useful information about a sample, but they can also be troublesome for the spectroscopist because they are a source of line-broadening in the NMR spectrum. This line-broadening happens as the decay time of the free induction decay (FID) signal is shortened by anisotropic effects that cause a loss of coherency among the magnetic moments of the nuclei in the sample.

For our study, we were focused on using NMR diffusion-imaging to elucidate details of a lipid membrane system. Use of this technique requires a solid-state NMR spectrum with narrow resonances, and therefore, required the removal of spin-spin dipolar coupling (also referred to as "dipole-dipole" or simply "dipolar" coupling), an anisotropic effect that arises from the magnetization of two nuclei interacting through space. This dipolar coupling effect can be hetero- or homonuclear, and it is commonly removed by magic-angle spinning (MAS). However, it is also possible to remove this effect via MP-NMR, using a well-choreographed series of radio frequency (*rf*) pulses. Before discussing the differences between the MAS and MP-NMR as decoupling techniques, a closer look at anisotropic effects is required.

A summary of the internal and external effects that are experienced by nuclei in different types of NMR samples is shown in Figure 2. In the table are the external effects that are used as experimental controls, and the internal interactions that affect the NMR spectrum. The relative sizes of the circles demonstrate the magnitude of each interaction, *e.g.* in solids, dipolar coupling has a greater effect on the NMR spectrum than chemical shift anisotropy (CSA). The absence of a circle for dipolar coupling in isotropic liquids indicates there is no dipolar coupling seen for that type of sample. Dipole-dipole coupling is not observed in isotropic liquids because anisotropic effects are orientation and time dependent. The increased degrees of freedom in an

isotropic liquid allow greater molecular motion, and the increased motion results in an averaging of the anisotropic effects to zero, as the molecules are constantly reoriented. In anisotropic liquids, which have distinct phase separations, the motion of molecules is limited, and effects such as dipolar and quadrupolar coupling are observed. When the effect of an experimental control is greater than the effect of an internal interaction, that control may be used to reduce or eliminate the effects of that interaction. Hence, in liquid-crystals (which are anisotropic liquids), MAS may be used to reduce or eliminate dipolar coupling effects from the NMR spectrum.

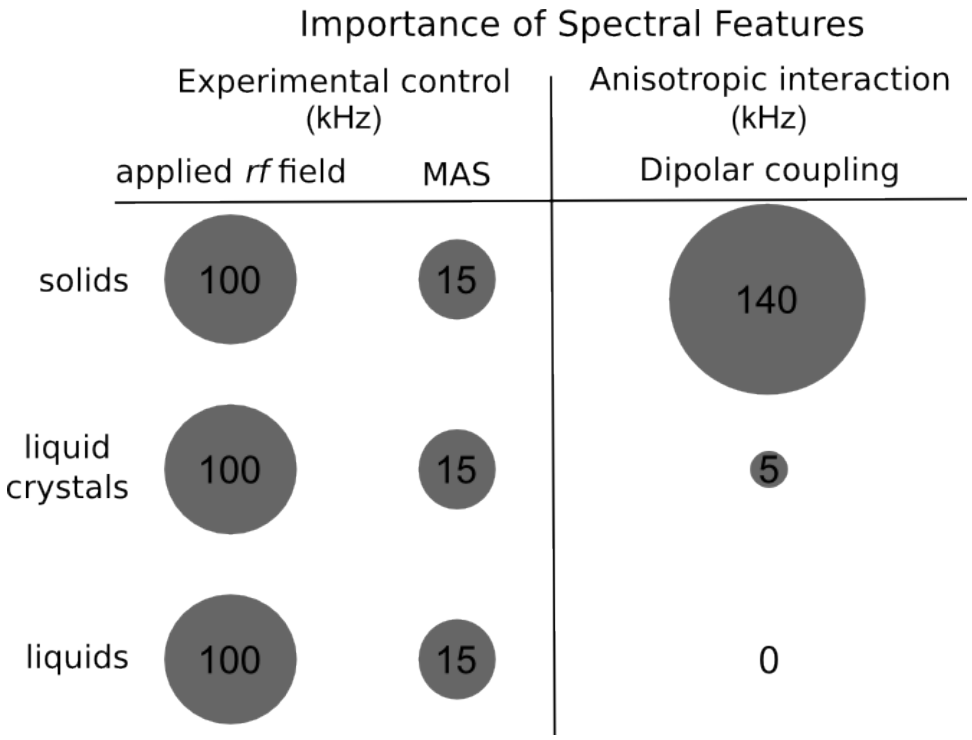

Figure 2: Manipulating anisotropic ^{1}H NMR spectral features. The diagram shows the magnitude of various effects experienced by different types of samples during an NMR experiment. The relative sizes of the circles indicate which interactions produce the most noticeable effects; if an experimental control has a greater effect than an internal interaction, then that control can be used to eliminate or reduce that interaction.

In the work presented here, detection of the ^{1}H signal was desired, and therefore, it was necessary to remove the homonuclear dipolar coupling effects from the NMR spectra. Our goal was to produce an NMR spectrum with signal-to-noise (S/N) that is sufficient for observing the diffusion of lipids in the bilayer. The Hamiltonian that dictates the dipole-dipole coupling observed in the NMR spectrum of a homonuclear spin pair is given as:

$$\hat{H}_{DD}^{jk} = \hat{H}_{spatial}\hat{H}_{spin} \propto \left(\frac{3\cos^2(\Theta_{JK})-1}{2}\right)(3\hat{I}_{jz}\hat{I}_{kz}-\hat{\mathrm{I}}_j\cdot\hat{\mathrm{I}}_k) \qquad (1)$$

where the first term in Equation 1 is the spatial factor of the interaction between two nuclear magnetic spins, *j* and *k*, showing the dependence on Θ_{jk}, the angle between the internuclear vector and the external magnetic field (Figure 3). The second term, $(3\hat{I}_{jz}\hat{I}_{kz}-\hat{\mathrm{I}}_j\cdot\hat{\mathrm{I}}_k)$ is the spin factor, showing the magnetic interactions between the nuclei that contribute to the dipolar coupling.

B. MAS AND MP-NMR: LINE-NARROWING METHODS

By reducing the magnitude of, or eliminating altogether, the dipole-dipole interactions occurring in the sample, the line-broadening in the NMR spectrum will be reduced, providing higher resolution results and greatly improved signal-to-noise. Two approaches have been developed to provide homonuclear dipolar decoupling: MAS and MP-NMR. When Θ_{jk} approaches 54.7°, the spatial term of the Hamiltonian (Equation 1) approaches zero, effectively eliminating the dipolar coupling;[8] hence, this angle is referred to as the magic angle. By spinning the sample about an axis that is oriented at the magic angle, each revolution of the MAS rotor will project the internuclear vector onto the spinning axis, causing the spatial term of the dipole-dipole Hamiltonian to go to zero, thereby removing the dipole-dipole coupling effects from the NMR spectrum (Figure 3).

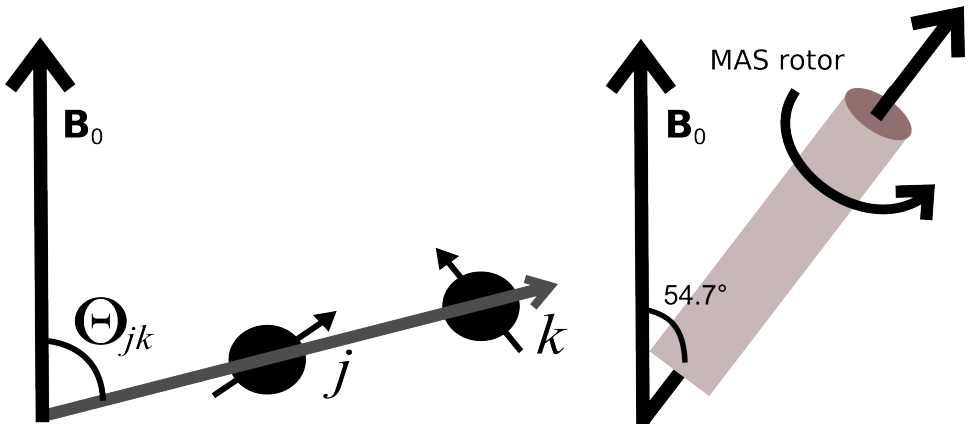

Figure 3: Anisotropy of dipole-dipole coupling removed by MAS. On the left, spins *j* and *k*, are interacting through space, and the angle of their interaction relative to the external field, $\boldsymbol{\Theta}_{jk}$, is shown. On the right, as the rotor spins about its axis along the magic angle, the average position of the internuclear vector becomes a projection onto the spin axis of the rotor, causing the average $\boldsymbol{\Theta}_{jk}$ to be the magic angle, 54.7°.

As mentioned earlier, the spin factor in the homonuclear Hamiltonian can also be manipulated via multi-pulse NMR. Dipolar coupling effects can be eliminated from the NMR spectrum by using a series of well-orchestrated *rf* pulses to interfere with the evolution of the spins, systematically reorienting the magnetization of the sample in between the acquisition of data points in the NMR signal.[9] These two techniques can be deployed separately or in tandem, to produce an NMR spectrum with enhanced resolution and spectral features similar to that of an isotropic liquid (Figure 2).

An MP sequence can be described as consisting of n cycles, each with μ subcycles. Figure 4 illustrates the MREV8 sequence which contains two subcycles, each comprised of a series of four phase-cycled *rf* pulses. The magnetization evolves following each *rf* pulse, during the period τ, and it continues to evolve until the next pulse is executed. The shorter the cycle time used, the better the line-narrowing defects provided by the pulse sequence will be.

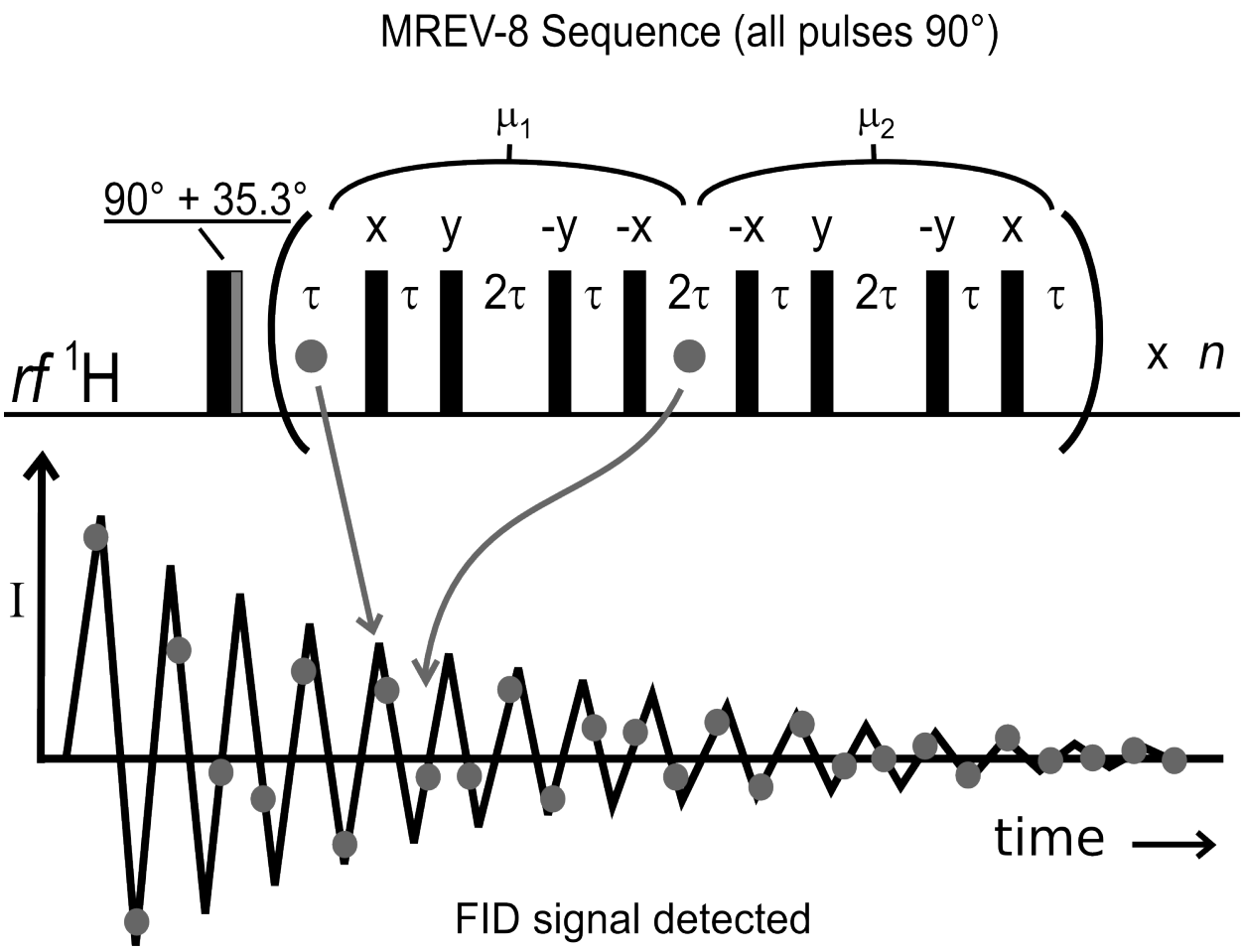

Figure 4: FID detected via windowed acquisition. The illustration shows an FID signal with the gray dots representing the data points where ^{1}H signal is detected. Applying *rf* pulses in between data point collection is known as *windowed acquisition*. The close proximity of pulses and data point detection presents a risk to the signal detection hardware. Above the FID, a simple pulse-and-detect application of the MREV8 sequence is shown. The sequence is repeated for *n* cycles, with two data points collected per cycle, until enough data points have been sampled to reconstruct the FID and obtain an NMR spectrum. In between each data point, one subcycle of the MREV sequence is applied, with τ typically less then 5 μs.

C. MULTI-PULSE NMR: BACKGROUND & EXPLANATION

Multi-pulse NMR has been used for several decades, stemming first from research in the late 1960s and 1970s.[10] The MP-NMR decoupling technique involves the application of a repeated series of *rf* pulses (referred to as a pulse sequence) that have an optimized timing and pulse phase cycle. Conventional solid-state NMR experiments allow the magnetization of the sample to precess at a frequency determined by the applied field and internal effects. In contrast, MP-NMR uses the *rf* pulses to alter the spin precession, preventing its quick decay. Several pulse sequences have been designed to reduce anisotropic line-broadening (WAHUHA, MREV8, BR-24) in NMR,[11] and have been used in MRI.[12] A closer examination of multi-pulse NMR requires an explanation of the spin density matrix and average Hamiltonian theory.

D. THE DENSITY MATRIX: DESCRIBING SPINS

To describe the state of a given spin system, it is convenient to use a density operator, $\hat{\rho}$. The density operator is a matrix describing the overall nuclear spin state of the sample at any point in time, avoiding the need to examine each spin individually.[8, 10-11] Nuclei within an NMR sample may have an average overall magnetic spin moment aligned with the applied field, in state $|\alpha\rangle$, or against it, in the $|\beta\rangle$ state, illustrated in Figure 5. Each of the individual spins may be considered to be in a superposition of those two states, but there will be some overall average alignment of spins at thermal equilibrium. The greater the percentage of a sample's nuclear spins there are aligned with $\mathbf{B}_0$, the better the NMR signal will be, as the alignment will increase the difference between the populations $\rho_{\alpha\alpha}$ and $\rho_{\beta\beta}$. Hence, the density operator is a powerful tool that lets the spin system be conveniently described by just four numbers, in the case of a sample of spin-1/2 nuclei.[8]

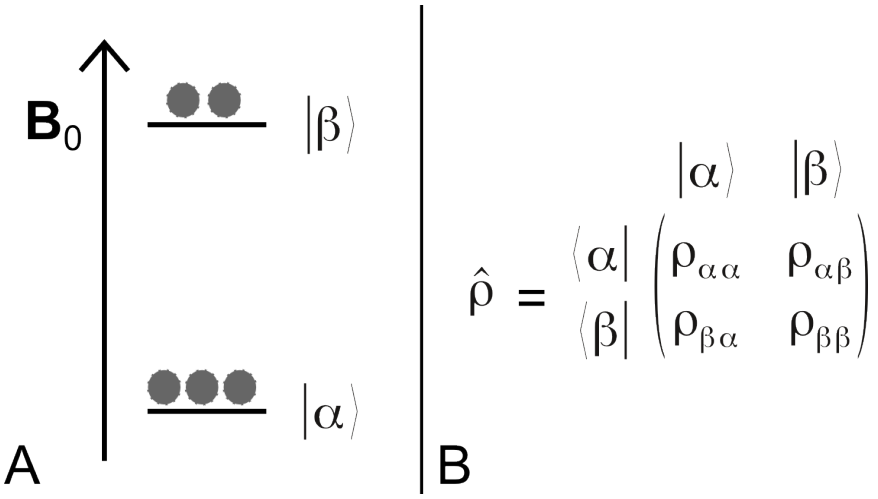

Figure 5: The Spin States and Density Operator Matrix. Side A of the illustration shows the two spin states in a sample in the applied field, $\mathbf{B}_0$. The β state is higher in energy, and therefore has a smaller population than the α state. Side B shows the density operator, $\hat{\rho}$, and its elements. The diagonal elements are the populations of the two spin states, and the off-diagonal elements are the coherences between the two states. The coherences indicate the presence of magnetization in the *xy*-plane. The greater the difference of the two populations, the more transverse magnetization there will be after the application of an *rf* pulse.

The populations are the diagonal elements in the density operator matrix for a system of non-interacting 1/2-spins:

$$\hat{\rho} = \begin{pmatrix} \rho_{\alpha\alpha} & \rho_{\alpha\beta} \\ \rho_{\beta\alpha} & \rho_{\beta\beta} \end{pmatrix} \quad (2).$$

Each of the off-diagonal elements, $\rho_{\alpha\beta}$ and $\rho_{\beta\alpha}$, represent the coherences between the $|\alpha\rangle$ and $|\beta\rangle$ states. Before an *rf* pulse is applied, there are no coherences, as there is no net transverse magnetization from the sample:

$$\hat{\rho} = \begin{pmatrix} \rho_{\alpha\alpha} & 0 \\ 0 & \rho_{\beta\beta} \end{pmatrix} \quad (3)$$

If the spin system is manipulated via a single *rf* pulse, its state will become time-dependent, according to:

$$\hat{\rho}(t) = \hat{U}(t)\hat{\rho}(0)\hat{U}(t)^{-1} \quad (4)$$

in which the propagator, $\hat{U}(t)$, has the form:

$$\hat{U}(t) = \exp(-i\hat{H}t) = \exp(-i\omega_{rf}\hat{I}_x) \quad (5)$$

The time-dependence of the density operator is illustrated in Figure 6. It is assumed in Equation 5 that $\hat{H}$ is constant from 0 to *t*, but in in the case of MP NMR, the Hamiltonian changes with each applied pulse and the magnetization evolves during each delay.[10-11] Figures 6 and 7 show how the Hamiltonians and therefore the density operator change as different events occur during an NMR experiment. When the state of the spins in the sample is known for a given point in time, it is possible to predict the form of the density operator. Because the Hamiltonians affecting the spin system under our experimental conditions are known (or can be reasonably approximated), $\hat{\rho}$ does not have to be calculated explicitly at each point in time, it may be predicted using average Hamiltonian theory.

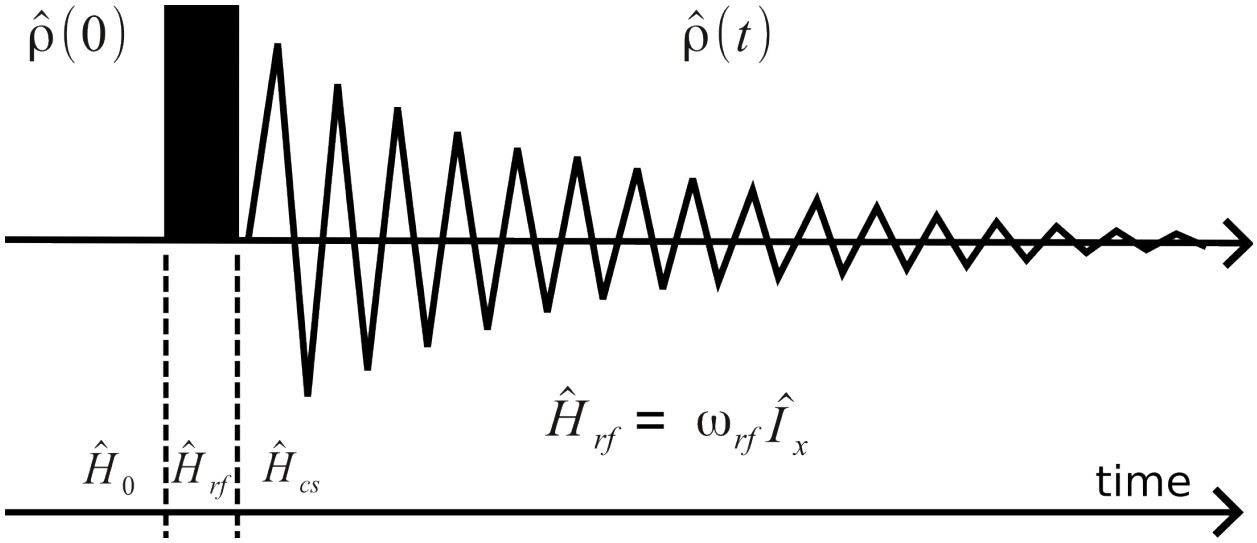

Figure 6: The Density Operator Becomes Time-dependent. The illustration shows how the density operator changes after the application of an *rf* pulse to the NMR sample. Likewise, the Hamiltonian affecting the system changes during the experiment. Because the form of $\hat{H}_{rf}$ is known, $\hat{\rho}(t)$ can be calculated.

E. USING AVERAGE HAMILTONIAN THEORY TO SIMPLIFY MP NMR

Across the entire period of the MP-NMR pulse sequence's cycle, *t*, there are several different Hamiltonians that will each describe the changing spin system at certain points in time. Figure 7 shows how the pulse sequence can be broken down into segments of time, each with its own Hamiltonian acting on $\hat{\rho}$. At the end of the cycle, a single Hamiltonian, that is an average of all the previous Hamiltonians that are contained within the cycle, will describe the state of the system. If there is a desired form for $\hat{\rho}(t_n)$, then a combination of pulses and delays can be used to exploit various Hamiltonians in order to obtain the desired state. In this way, it is possible to create a pulse sequence whose average Hamiltonian leaves out undesired effects, such as homonuclear dipole-dipole coupling, by building a cycle of pulses and delays whose individual Hamiltonians combine to cancel-out the terms of the unwanted interactions.

The density operator during a MP NMR experiment takes the following form, which shows the different Hamiltonians for each period in the pulse sequence and expresses them as an average:

$$\hat{U}(t) = \exp(-i\hat{H}_n t_n) \ldots \exp(-i\hat{H}_1 t_1) \quad (6)$$

$$\hat{U}(t) = \exp(-i\bar{H}t) \quad (7)$$

In this case, each time period in Equation 3 corresponds to the events taking place during the pulse sequence (as shown in Figure 7), and $t = (t_1 + t_2 + \ldots + t_n)$. The average Hamiltonian, $\bar{H}$, is the sum of all the previous Hamiltonians, averaged over the relevant interval of time, as shown below in Equation 10. The Hamiltonians in Equation 6 should appear in chronological order to account for the order of the *rf* pulses in the sequence.

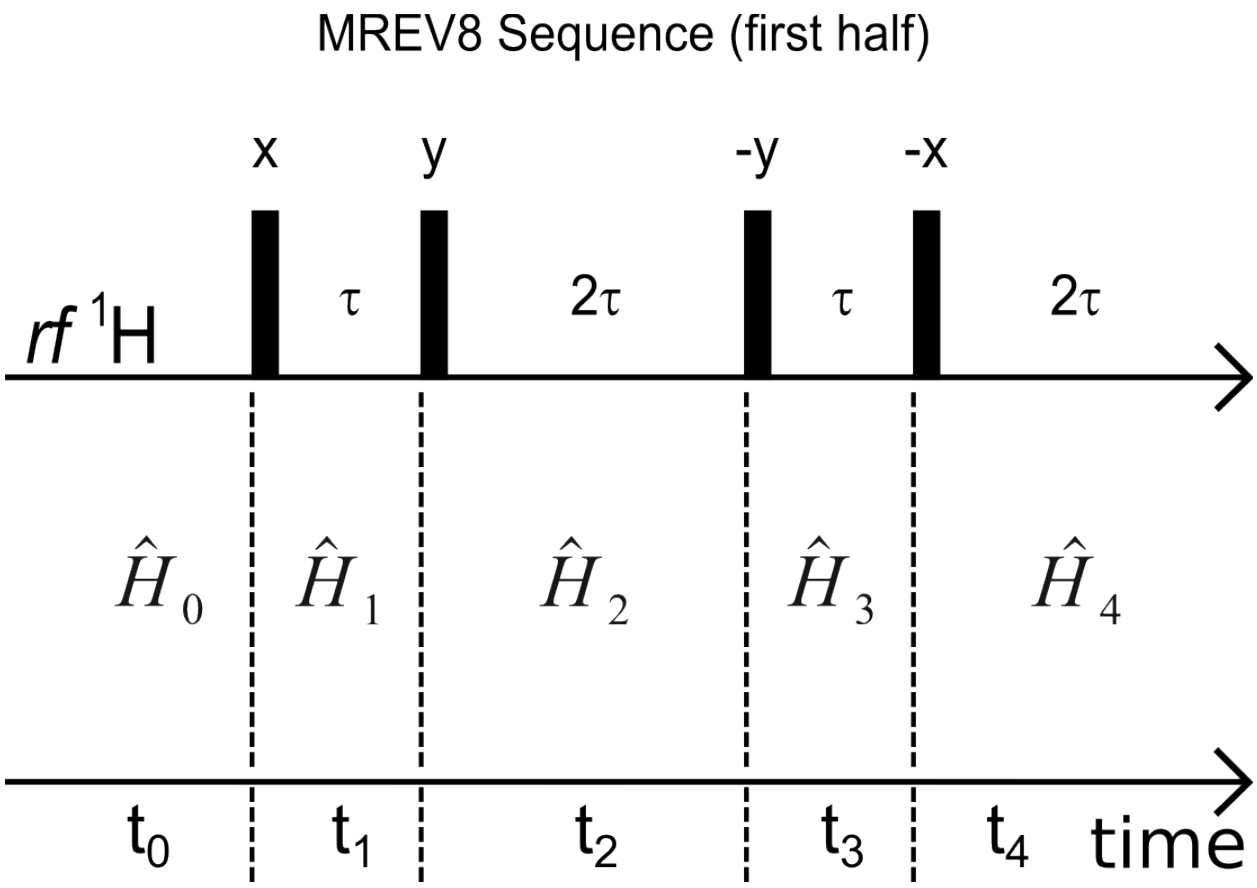

Figure 7: Hamiltonians during the pulse sequence. The illustration shows the different Hamiltonians affecting the spin systems at various points in time during the first half of the MREV8 pulse sequence. To more easily predict the state of the system at t_4, an average Hamiltonian, which will be comprised of all the previous Hamiltonians, can be calculated.

For a given pulse sequence, the average Hamiltonian, $\bar{H}$, can be calculated via Magnus expansion:[11]

$$e^{\hat{A}}e^{\hat{B}}=\exp\left\{\hat{A}+\hat{B}+\frac{1}{2!}[\hat{A},\hat{B}]+\frac{1}{3!}([\hat{A},[\hat{A},\hat{B}]]+[[\hat{A},\hat{B}],\hat{B}])+...\right\} \quad (8).$$
$$[\hat{A},\hat{B}]=\hat{A}\hat{B}-\hat{B}\hat{A}$$

For Equation 3:

$$\bar{H}(t)=\bar{H}^{(0)}+\bar{H}^{(1)}+\bar{H}^{(2)}+... \quad (9)$$

$$\bar{H}^{(0)}=\frac{1}{t}\left\{\hat{H}_1 t_1+\hat{H}_2 t_2+...+\hat{H}_n t_n\right\} \quad (10)$$

$$\bar{H}^{(1)}=-\frac{i}{2t}\left\{[\hat{H}_2 t_2,\hat{H}_1 t_1]+[\hat{H}_3 t_3,\hat{H}_1 t_1]+[\hat{H}_2 t_2,\hat{H}_3 t_3]+...\right\}$$

$$\bar{H}^{(2)}=-\frac{1}{6t}\left\{[\hat{H}_3 t_3,[\hat{H}_2 t_2,\hat{H}_1 t_1]]+[[\hat{H}_3 t_3,\hat{H}_2 t_2],\hat{H}_1 t_1]+\frac{1}{2}[\hat{H}_2 t_2[\hat{H}_2 t_2,\hat{H}_1 t_1]]\right. \quad (11)$$
$$\left.+\frac{1}{2}[[\hat{H}_2 t_2,\hat{H}_1 t_1],\hat{H}_1 t_1]+...\right\}$$

The first order term in Equation 9 is simply the average of the Hamiltonians that occur during the cycle of the pulse sequence. The higher order terms of Equation 11 are corrections to the first-order term that contain commutators, and if the Hamiltonians commute, these higher order terms can be neglected.[10-11] In the case where only the first-order term needs to be considered, the analytic form of the approximate average Hamiltonian can be determined and useful details of the pulse sequence's operation on a spin system can be ascertained. The use of a toggling reference frame will allow non-commuting terms to be eliminated, simplifying the description of the pulse sequence's effects on the sample.

The MREV8 pulse sequence is a typical MP-NMR sequence that as designed to eliminate dipole-dipole coupling interactions. It is assumed that the *rf* pulses are on resonance and of sufficient power so that dipole-dipole coupling during the pulse and the effects of the applied magnetic field, $\mathbf{B}_0$, do not need to be considered. During the delays, the magnetization evolves only due to internal spin interactions. The Hamiltonians during the delays should consist only of the Hamiltonian for homonuclear dipole-dipole coupling:

$$\hat{H}_{dip} = \sum_{i>j} B_{ij} \left(3\,\hat{I}_z^i \hat{I}_z^j - \hat{\mathbf{I}}^i \cdot \hat{\mathbf{I}}^j \right) \qquad (12)$$

where the label z is in reference to the rotating frame axis, and the term B_{ij} contains the spatial dependent factors, shown previously in Equation 1. Since the Hamiltonians over the interval of the MREV8 cycle do not all commute with each other, transformation into a toggling reference frame will be useful in this case. Specifically, the *rf* Hamiltonians do not commute with each other nor with the delay Hamiltonians. In the toggling frame, these non-commuting terms will vanish, and the mathematical description of the spin system will be simplified as the remaining Hamiltonians will commute.

Applying the toggling frame to the MREV8 pulse sequence, starting with the first subcycle, in the first time period, 0 to t_1, the magnetization is only evolving due to the influence of internal spin interactions. The Hamiltonian describing the evolution is the same as Equation 12:

$$\hat{H}\left(0 \rightarrow t_1\right) = \sum_{i>j} B_{ij} \left(3\,\hat{I}_z^i \hat{I}_z^j - \hat{\mathbf{I}}^i \cdot \hat{\mathbf{I}}^j \right) \equiv \hat{H}_{zz} \qquad (13)$$

the second period of free evolution, from t_1 to t_2, is described by:

$$\hat{H}\left(t_1 \rightarrow t_2\right) = \sum_{i>j} B_{ij} \left(3\,\hat{I}_y^i \hat{I}_y^j - \hat{\mathbf{I}}^i \cdot \hat{\mathbf{I}}^j \right) \equiv \hat{H}_{yy} \qquad (14).$$

Using this method to accumulate the effects of all the pulses and delays, the average first-order Hamiltonian for the first subcycle of the MREV8 sequence is:

$$\bar{H}^{(0)} = \frac{\hat{H}_{zz}\,\tau + \hat{H}_{yy}\,\tau + 2\,\hat{H}_{xx}\,\tau + \hat{H}_{yy}\,\tau + \hat{H}_{zz}\,\tau}{6\,\tau} \qquad (15)$$

where

$$\begin{aligned} \hat{H}_{zz} + \hat{H}_{yy} + \hat{H}_{xx} &= \sum_{i>j} B_{ij} \left[\left(3\,\hat{I}_z^i \hat{I}_z^j - \hat{\mathbf{I}}^i \cdot \hat{\mathbf{I}}^j \right) + \left(3\,\hat{I}_y^i \hat{I}_y^j - \hat{\mathbf{I}}^i \cdot \hat{\mathbf{I}}^j \right) + \left(3\,\hat{I}_x^i \hat{I}_x^j - \hat{\mathbf{I}}^i \cdot \hat{\mathbf{I}}^j \right) \right] \\ &= \sum_{i>j} B_{ij} \left[\, 3\left(\hat{I}_z^i \hat{I}_z^j + \hat{I}_y^i \hat{I}_y^j + \hat{I}_z^i \hat{I}_z^j \right) - 3\,\hat{\mathbf{I}}^i \cdot \hat{\mathbf{I}}^j \right] \equiv 0 \end{aligned} \qquad (16).$$

Equations 15 and 16 show that there is no net homonuclear dipole-dipole interaction to first-order at the end of the first MREV8 subcycle. Detecting the sample magnetization at this point will give an FID showing chemical shift effects, but no dipolar coupling.

The next MREV8 subcycle applies pulses having the same timing as the first but with a different ordering of $\hat{H}_{zz}$, $\hat{H}_{yy}$, and $\hat{H}_{xx}$. The effect of the second subcycle is then the same as the first: the dipole-dipole interactions are removed from the NMR spectrum. Because the delay between the two subcycles is so small, only a single data point from the FID signal is acquired during this window, and then the pulse sequence is repeated until enough data points have been acquired to reconstruct the complete FID. In this pulse sequence, at the end of each subcycle, the sample magnetization is returned to the same state in which it was at the start of the pulse sequence. This creates a convenient window during the decoupling cycle at which the sample magnetization can be detected and a coherent FID signal may be recovered (this window is shown in Figure 4).

It is the rapid re-orienting of the density operator, along with the use of a phase cycle which is designed to have the later pulses in the sequence reverse the effects of the earlier pulses, that results in an average dipole-dipole Hamiltonian of zero magnitude and eliminates the dipolar coupling effects from the NMR spectrum. If the phase-cycle were altered, then later pulses in the pulse sequence may not undo the effects of earlier pulses, resulting in a non-zero dipole-dipole Hamiltonian. Likewise, deviation from perfect, 90° pulses or deviation from resonance can result in residual dipolar effects broadening lines in the NMR spectrum.

F. LIMITATIONS OF MP NMR FOR LINE-NARROWING

There are, naturally, limitations to the line-narrowing provided by MP-NMR. Up until now, it has been assumed that the pulses in the MP NMR experiment were on-resonance, meaning the carrier frequency of the *rf* pulses was equal to the magnetic resonance frequency of the nuclei in

the sample, ω. In practice, the *rf* pulses may be transmitted on a carrier frequency that is different than ω, where the difference between the carrier frequency and Δω is called the resonance-offset.

A detailed description of the limits of resolution has been written by Garroway, Mansfield, and Stalker.[10] The experimental concerns when using MP-NMR include the duty cycle of the *rf* coil (the ratio of time when the *rf* is on *c.f.* time when it is off), the cycle time of the selected pulse sequence, and the resonance-offset of the carrier frequency. The line-narrowing is known to be related to the cycle time and carrier frequency. In the case of CaF_2, when the carrier frequency is moved to about 0.5-1.3 kHz off-resonance, maximum line-narrowing is seen, and the linewidth observed is reported to show a τ^4 dependence.[10, 13-14] At about 1.4 kHz off-resonance, the linewidth is observed to have a τ^2 dependence.[10]

The resolution achievable via MP NMR is primarily limited by residual dipole-dipole interactions that are left over after the previously described averaging. These residual interactions result in non-uniform line broadening in which the linewidth is dependent on the deviation of the *rf* pulses from resonance (resonance offset). In general, how the broadening depends on resonance offset will vary with the pulse sequence used, but overall, a change in line-narrowing ability by a factor of 3 will occur when the carrier frequency is moved to about 3 kHz off-resonance.[10]

Pulse sequences can be designed to compensate for the residual broadening terms that are left over in the Hamiltonian. In the case of MREV8, the sequence is divided into two subcycles, each containing a third-order dipole-dipole coupling term (that is itself comprised of several terms). However, the residual dipole-dipole terms at the end of each subcycle should be opposite in sign and equal in magnitude, and therefore, the sequence is self-compensating.

If an exponential approximation is used for modeling the signal decay, the pure dipole-dipole coupling term contained within the residual third-order term, $\left(\bar{H}^{(2)}\right)_{d^3}$, contributes to line broadening according to:

$$W_{d^3} \propto \tau^4 / |\Delta\omega| \qquad (17)$$

which shows that linewidth should be reduced as resonance offset is increased.[10] In Equation 17, $\Delta\omega$ is the resonance offset, and τ is the delay period between the *rf* pulses in the MREV8 sequence. The narrowing effect produced by $\left(\bar{H}^{(2)}\right)_{d^3}$ is known as "second averaging" or "offset narrowing." The $\left(\bar{H}^{(2)}\right)_{d^2c}$ term predicts that linewidth should *increase* with increasing resonance offset, in contrast to the pure dipolar term. These two terms compete and create two distinct relationships between linewidth and the resonance-offset. In one region, the pure dipolar term dominates, and the linewidth follows the τ^4 dependence. In the second region, the mixed term makes a greater contribution, creating a τ^2 dependence.

In contrast to the exponential approximation, a Gaussian function can be used to approximate the signal decay. Using this method, the contribution to linewidth from the pure-dipolar term is:

$$W_{d^3} \propto \tau^2 \qquad (18).$$

Equation 18 does not contain the $\Delta\omega$ term, indicating that linewidth may not depend explicitly on resonance offset. The mixed terms still contain the resonance-offset dependence, but they, like Equation 18, predict that line broadening goes as τ^2 instead of τ^4. The competing terms in the third-order dipole-dipole coupling function result in a non-linear linewidth dependence on resonance offset and cycle time. Regardless of the exact dependence of linewidth on $\Delta\omega$, the use of shorter τ, and therefore a shorter cycle time, should give narrower lines in the NMR spectrum.

G. THE USE OF MAGNETIC FIELD GRADIENTS IN MRI AND NMR MICROSCOPY

The line-narrowing techniques outlined allow the implementation of conventional MRI techniques developed for solution-state NMR. This work is focused on using MP-NMR with PGSTE-NMR to measure the diffusion of lipids in a bilayer, and our goal has been to use MP-

NMR in place of MAS because there is an inherent incompatibility between the use of pulsed gradients and MAS.[15]

The signal in NMR arises from the precession of magnetic moments in the sample, and the frequency of that signal, ω, is dependent on the strength of the applied magnetic field, B_0, and gyromagnetic ratio, γ, according to the equation:

$$\omega = \gamma B_0 \qquad (19).$$

In MRI, the frequency is dependent on location, and the signal response from the sample will be a distribution of frequencies that are position-dependent (Figure 5):

$$\omega(z) = \gamma\left(B_0 + z\frac{\partial B_z}{\partial z}\right) \qquad (20)$$

where z is the location of a molecule and $\frac{\partial B_z}{\partial z}$ is the magnetic field gradient.

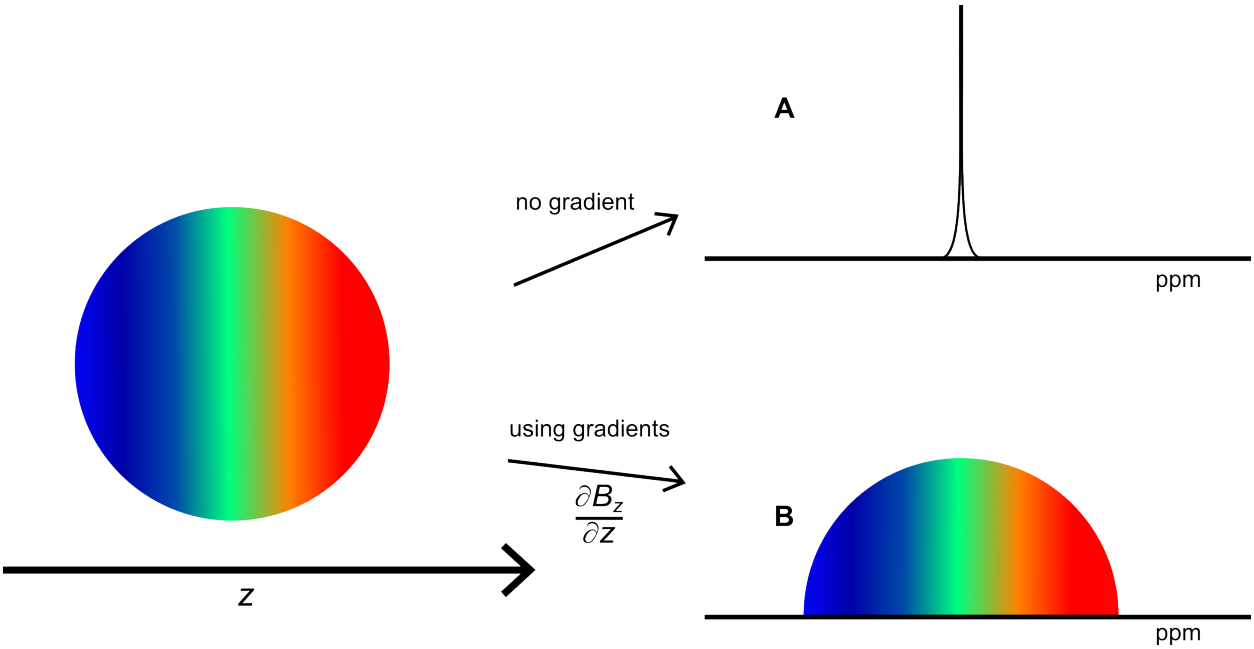

Figure 8: Magnetic field gradients encode spatial information into the NMR spectrum. On the left, an irregularly shaped object with only a single resonance is subjected to a gradient field, shown as a spectrum of color. On the right, two NMR spectra are shown for the object; the top spectrum shows an isotropic signal, while the lower spectrum shows anisotropic signal that reflects the shape of the object. Each slice of the object on the left corresponds to a different color in the spectrum on the right.

Figure 8 shows an irregularly shaped object that contains only a single magnetic resonance. In a uniform magnetic field, the NMR spectrum for the sample will contain only a single peak, as seen in spectrum A in Figure 8. However, when there is a magnetic field gradient, the precession frequencies of the nuclei in the sample become position-dependent (Equation 20), illustrated by the spectrum of color spread over the sample area. The gradients used for imaging encode position-dependent information into an NMR spectrum by varying the strength of the magnetic field along one or more spatial axes of the sample.[8, 9] The NMR spectrum will then convey spatial details of the sample, as shown in spectrum B, Figure 8. If the applied field-gradient, $\frac{\partial B_z}{\partial z}$, is large, then small changes in position will result in large changes in $\omega(z)$. For MRI, gradients are applied in each spatial direction to allow the construction of a detailed 3-dimensional image, with a resolution on the order of 0.1 mm.[9]

The use of a pulsed-field gradient requires the presence of gradient coils in the NMR probe, and MAS requires a set of pneumatics to spin the sample, contained within a stator, inside the probe. On a gradient-equipped MAS-NMR probe, the gradient coils are positioned outside of the stator, while the pneumatics are contained within. The competition for space inside the NMR probe gives rise to the incompatibility of MAS and strong magnetic field gradients. A schematic of a typical gradient-equipped MAS stator is shown in Figure 9, with the pneumatics represented by the black lines running through the interior of the stator. In Figure 9, the gradient coils are shown as two copper-colored rings, positioned on the outside of the stator. In this configuration, the gradient coils are 2-3 cm apart (the length of the stator). Better placement of the gradient coils would have them along the sides of the rotor cavity, which would place them about 4-5 mm apart, as further examination of the distance-dependence of the gradient coils' efficacy will show.

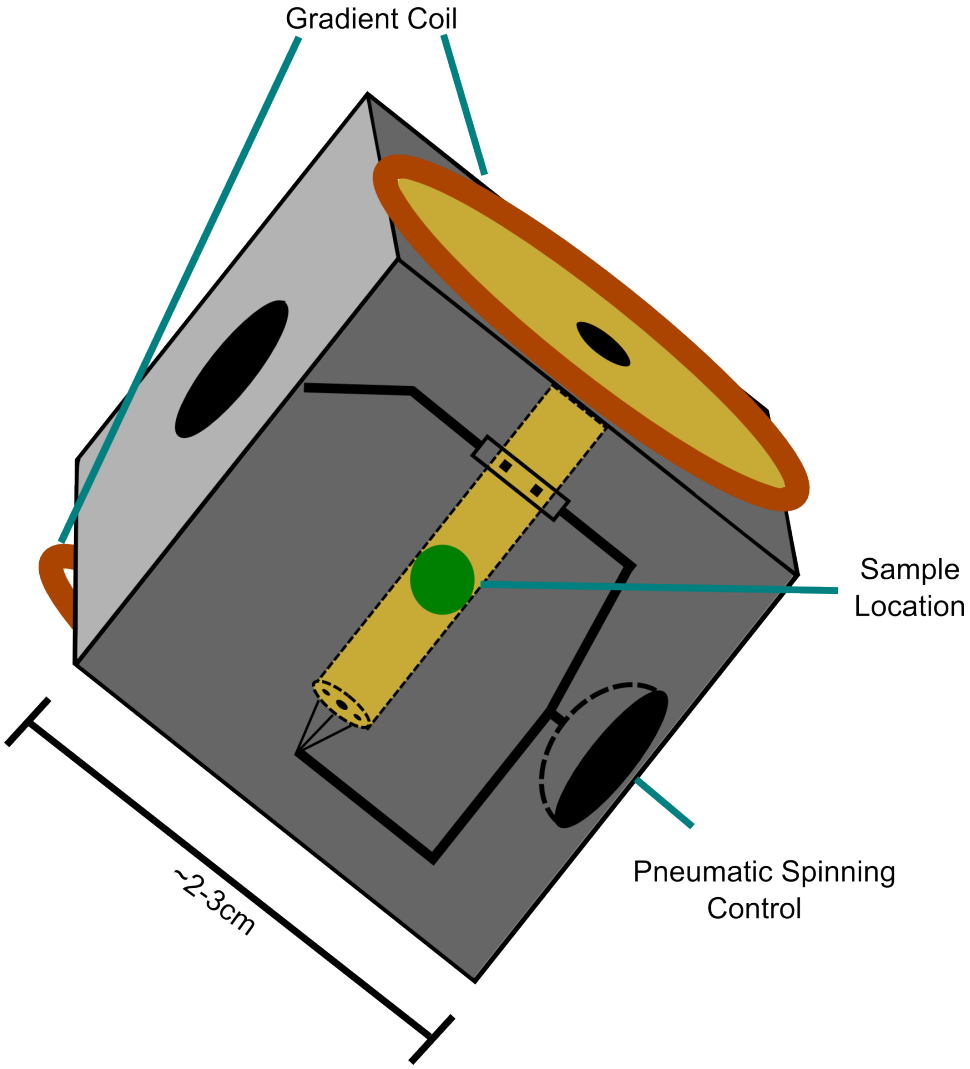

Figure 9: Gradient-equipped MAS stator from an NMR probe. Inside the stator are a series of ports that direct compressed air to the sample rotor (the rotor is not shown here). The spacing of the gradient coils is limited by the complex pneumatic system necessary to spin a 2 g rotor at speeds exceeding 20 kHz.

H. COMBINING MAS WITH GRADIENTS: THE INCOMPATIBILITY

The gradient coils are often a Helmholtz pair of wire coils that are positioned at each end of the stator in the probe (Figure 9). By applying opposing currents through each coil, a magnetic field gradient is created between them. The geometry of the pair is designed so that the magnetic field acting on the sample varies linearly along the spinning axis of the stator, because a non-linear gradient will create spatial misrepresentations in the image.[16] The spatial resolution of the imaging probe is improved when the spacing between the gradient coils is reduced.[17] To illustrate the relationship between the magnitude and geometry of the gradient coil, we will focus on the magnetic field at the center of the sample. The magnetic field will be varied, with the coils separated by a distance, Z_0, and, in order to simplify the illustration, the coils will be considered infinitely long in the x direction (reducing to a wire). At the point $x = y = z = 0$ (the center of the sample), the magnetic field along the z axis will be:

$$B_z = \frac{\mu_0}{2\pi}\frac{I_x}{Z_0^2}\frac{Y_0}{[1+(\frac{Y_0^2}{Z_0^2})]} \qquad (21)$$

where μ_0 is the permeability of free space, I_x is the applied current, Y_0 is the width of the coils, and Z_0 is half the distance between the coils. When the coil width is a fraction of the coil spacing, the gradient in the z direction is then the field derivative:

$$\frac{\partial B_z}{\partial z} = \frac{\mu_0}{2\pi}\frac{I_x}{Z_0^3}\frac{Y_0}{[1+(\frac{Y_0^2}{Z_0^2})]^2} \qquad (22).$$

As Equation 22 illustrates, if the coil separation, Z_0, is reduced by half, the result will be an increase in the gradient by a factor of approximately 6; the gradient generated by our amplifier would increase from 0.5 T/m to about 3.0 T/m.

In summary, the mechanical requirements associated with MAS hinder the ability to acquire high-resolution images. Using MP-NMR in place of MAS-NMR allows a probe design that does not require pneumatics for spinning a sample, and a probe without MAS hardware will allow improved design and placement of the gradient coils.

I. FREE AND CONFINED DIFFUSION

The diffusion constant, *D*, reflects the physical properties of the diffusing molecule and the environment it traverses. Any observed changes in *D* are indicative of either changes to the diffusing analyte or its surroundings. Hence, in an isotropic, homogeneous environment, free diffusion (and a single *D*) should be observed, regardless of the experimental parameters. Free diffusion in two dimensions is governed by the equation:

$$\langle x^2 \rangle^{1/2} = \sqrt{4\mathrm{D}\,\Delta} \qquad (23)$$

where $\langle x^2 \rangle^{1/2}$ is the mean-square displacement and Δ is the time allowed for diffusion. In a heterogeneous system, confined diffusion may be observed. In this case, after some time, Δ, the diffusing species will reach maximum possible displacement, as illustrated in Figure 1. Because the diffusion path is limited, the apparent diffusion constant is reduced as the displacement limit is reached. At longer diffusion times, the confined molecules do not appear to be diffusing, because the displacement plateaus. Time-dependent diffusion is a marker of a heterogeneous system, and by measuring time-dependent diffusion, the scale of the confinement can be resolved.

J. NMR DIFFUSION-IMAGING

Determining the organization of a lipid membrane system requires an imaging technique with spatial resolution that is beyond the resolution of conventional MRI and below the optical limit. Studying the time-dependent lateral diffusion of lipids via NMR can provide spatial detail on the order of 100 nm. In diffusion measurements, gradients are used to locate molecules before and after a diffusion time, Δ. To extract the diffusion constant, a single resonance is chosen from the NMR spectrum, and its attenuation due to increasing gradient strength is measured, using the PGSTE pulse program in Figure 10. The attenuation of signal, *I*, happens due to diffusion occurring between the spatial encoding and decoding periods of the PGSTE program (Figure 10), and the sensitivity of signal intensity to changes in position can be modulated by adjusting our experimental controls, which are collected as the parameter *k*. The attenuation of signal is related to the diffusion coefficient and *k* by the equation:

$$\ln\left(\frac{I}{I_0}\right) = -kD \qquad (24)$$

$$\text{where} \quad k \propto \gamma^2 g^2 \delta^2 \Delta \qquad (25),$$

I_0 is the signal intensity of the selected resonance without gradients, *g* is the gradient strength, and δ is the length of the position encoding and decoding gradient pulses.

Figure 10 shows a basic PGSTE NMR pulse program; it contains a series of *rf* pulses coordinated with gradient pulses. In the first part of the program, the nuclear magnetization is rotated into the transverse direction, perpendicular to B_0. During the spatial encoding time, a gradient is applied, causing the nuclei to begin precessing with position-dependent frequencies. In order to slow transverse relaxation of the magnetization during the diffusion time, the next *rf* pulse stores the position-dependent nuclear magnetization in the *z* direction, and the molecules are allowed to diffuse for the time Δ. With the application of a third *rf* pulse, and another gradient, the nuclear magnetization signal is measured. As *k* is increased, by varying δ, *g,* or Δ,

the attenuation observed should increase according to Equation 24. As shown in Figure 11, a plot of $\ln(\frac{I}{I_0})$ versus k is linear and the diffusion constant can be extracted from the slope. As referenced above in the discussion of free diffusion, changes in D under different experimental conditions will convey information about the spatial organization of the sample.

In an example of confined diffusion, Figure 11 shows diffusion constants measured for a single sample at three different diffusion times (Δ = 50, 200, and 700 ms). The sample in Figure 11 was a complex mixture of phosphatidylcholines (1.5/1.5/1/13 mol % DMPC/POPC/DHPC/cholesterol) that have been shown to form phase-separated lipid domains at 292 K. The diffusion measurements were made via ^{1}H PGSTE MAS-NMR, measuring the attenuation of the choline peak.[3] After measuring the attenuation as a function of gradient strength, the process is repeated with a series of increasing diffusion times, Δ. As Δ is increased, the decrease of the diffusion constant indicates confined diffusion within the bilayer (Figure 1), which is consistent with the formation of lipid domains. The change in D for this sample becomes more apparent in Figure 12, where we observe displacement as a function of diffusion time.

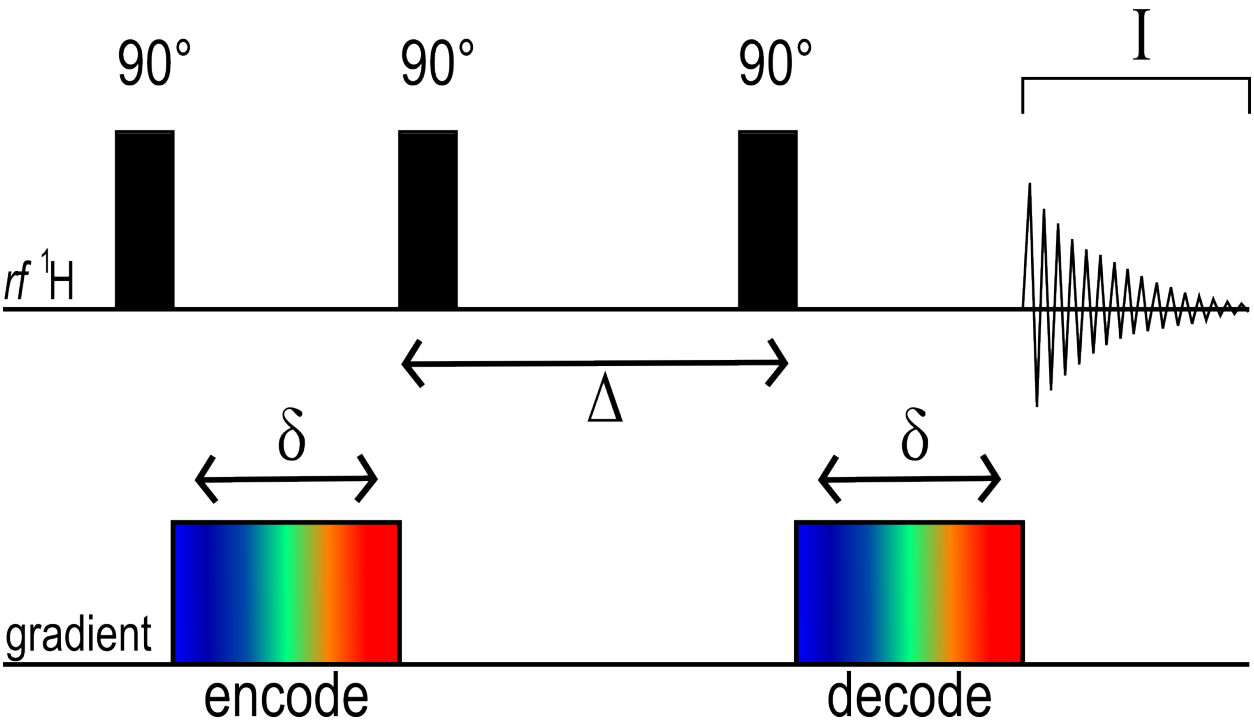

Figure 10: A basic PGSTE NMR pulse program. During the first gradient pulse, δ, an image of the sample is encoded into the sample magnetization. The second 90° pulse stores the image in the *Z* direction, and the second gradient pulse recovers the stored information. If diffusion occurs during the period Δ, the FID will have lowered intensity, *I*, when compared to the FID obtained without the use of gradients. Attenuation of the final signal, *I*, reflects the average motion of the spins.

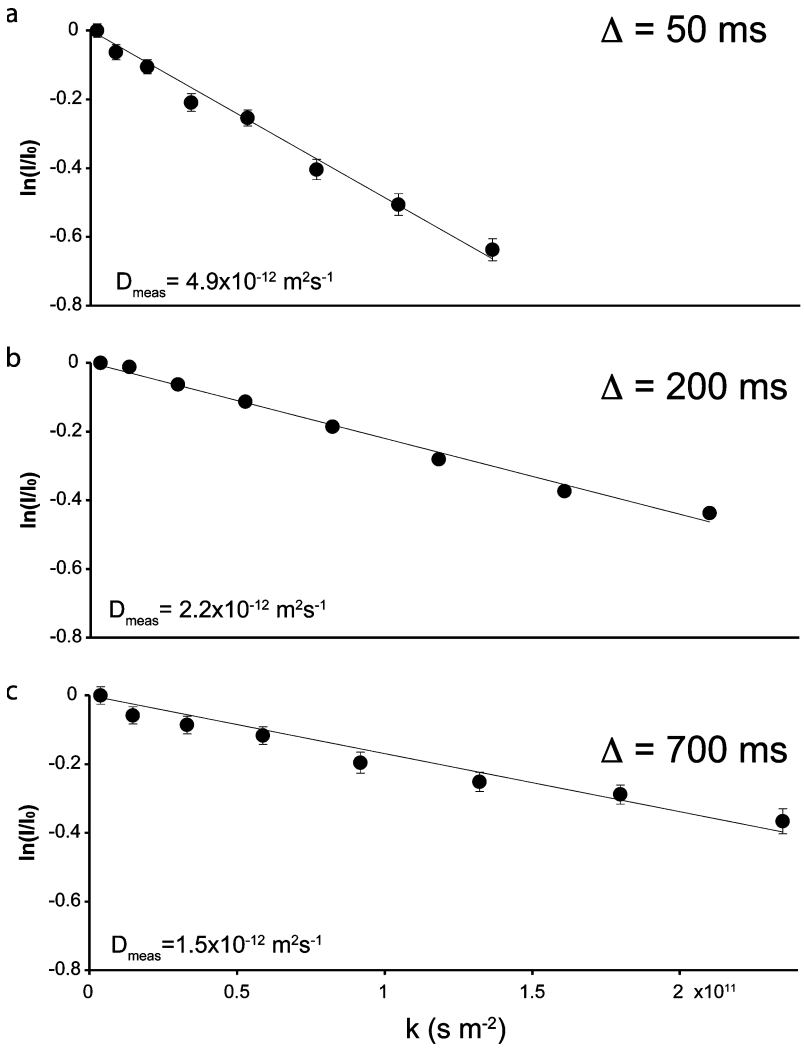

Figure 11: Bicelle sample shows lipid domains. The three plots show the diffusion coefficient, *D*, measured with increasing diffusion time, Δ. The slope is reduced as Δ is increased, because of the restricted diffusion present in the sample of bicelles at $T = 292$ K.[3]

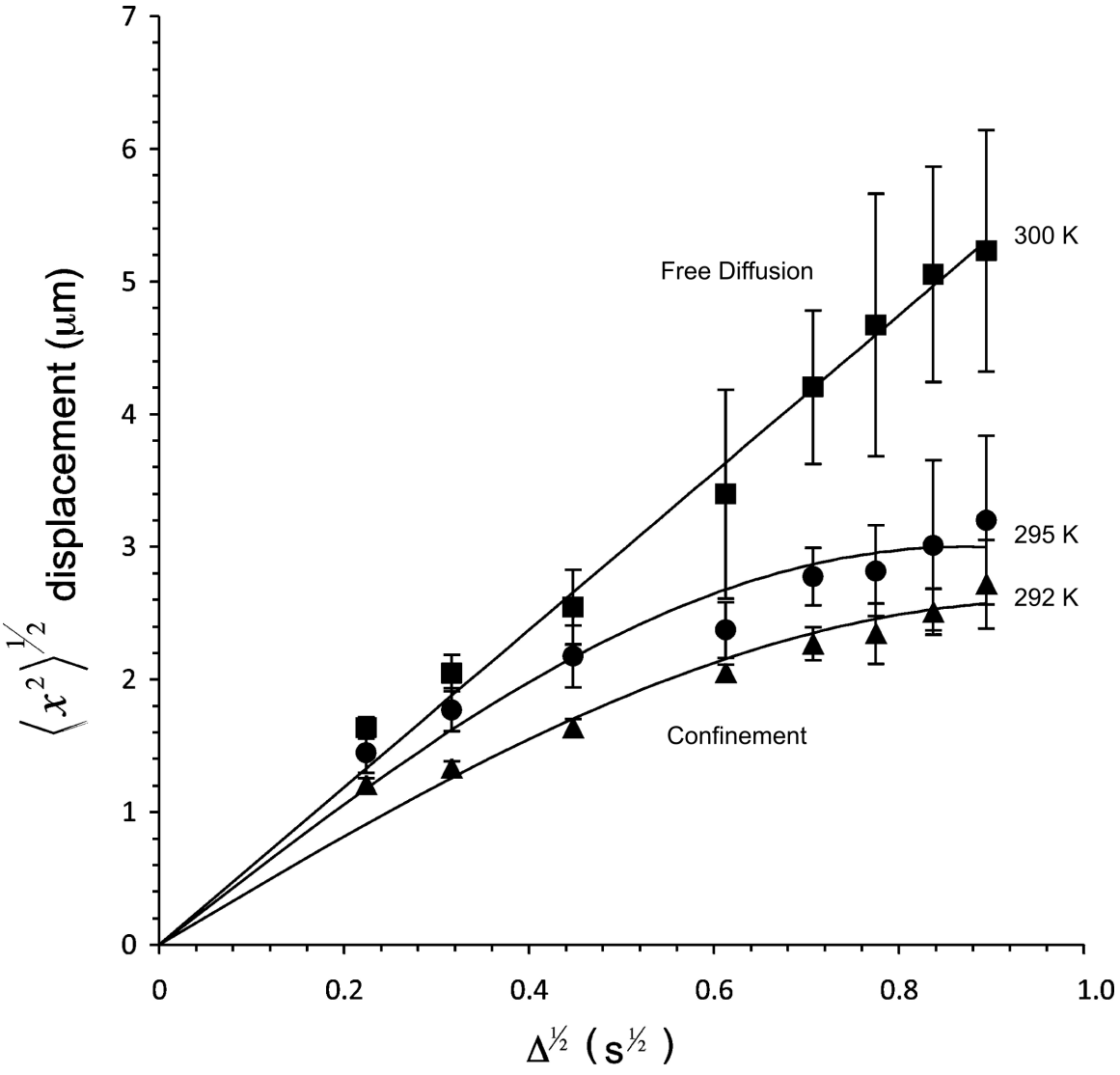

Figure 12: Diffusion measurement of lipid displacement reflects magnitude of confinement. The average displacements in 1.5/1.5/1/chol DMPC/POPC/DHPC unsaturated lipid system with and without domains as a function of diffusion time at three temperatures. At 300 K (■), the displacement increased as the square root of time, consistent with free diffusion. In contrast, at temperatures 295 K (●) and 292 K (▲), the lipid displacements are limited and showed plateaus, indicating confined diffusion within a lipid domain. Error bars reflect the fit uncertainty (±2σ) of the diffusion constant for each point.[3]

To view the change in diffusion constant in terms of average displacement, the mean-square displacement, $\langle x^2 \rangle^{1/2}$, is plotted versus the square-root of diffusion time, $\Delta^{1/2}$, using Equation 23. Such a plot will reveal whether there is free diffusion occurring in the sample or if there is some barrier restricting diffusion (Figure 11). The plots in Figure 11 were made from diffusion measurements of a single sample of domain forming bicelles at three different temperatures, and displays the average displacement as a function of diffusion time.

The sample in Figure 11 consisted of different lipid species with cholesterol, and the formation of ordered domains within the sample was caused by the difference in phase transition temperatures. When the sample was below the main-chain phase transition temperature, T_m, for the unsaturated lipids in the sample, the short and long chain lipids segregated. The domain formation is evidenced by the restricted diffusion observed at the lower temperatures (292 and 295 K). When the temperature was raised above the T_m of the saturated lipids (300 K), there was enough free energy to prevent domain formation, and free diffusion was observed.

As illustrated in Figure 12, a single diffusion constant describes the translational motion of a molecule that is unconfined, showing displacement that scales linearly with $\Delta^{1/2}$, but in the case of confined diffusion, the displacement values will plateau. The plateau will indicate the scale of the area to which the diffusing molecules are confined. The observed relationship between $\langle x^2 \rangle^{1/2}$ and $\Delta^{1/2}$ will no longer be linear, as it was in Equation 23.

Combining Equations 23 and 24 reveals that the use of stronger gradients will allow the use of shorter diffusion times during the experiment. The relationship between the smallest size of the domain that can be measured by PGSTE NMR and the gradient strength applied is:

$$r_{min} = \frac{2}{\gamma \delta g_{max}} \qquad (26)$$

where r_{min} is the minimum mean-square displacement observable, a direct measure of our spatial resolution. There are other benefits to using stronger gradients: a shorter diffusion time can be used, which will reduce the amount of signal lost to relaxation during Δ. Currently, the hardware

in our laboratory, which is a commercially produced, gradient-equipped, solid-state NMR probe, has a g_{max} of about 0.5 T/m, which allows a resolution down to several hundred nanometers when observing attenuation of ^{1}H signal. The use of a commercially made NMR diffusion-imaging probe can provide a gradient on the order of 50 T/m, providing a resolution better than 100 nm.

K. COMBINING MP-NMR AND DIFFUSION-IMAGING

In order to implement diffusion measurements using MP-NMR, our work required the assembly of an MP-PGSTE NMR pulse program. Our program was constructed with the aid of Drs. Hans Foerster, Althoff Gerhard, and Jochem Struppe, and with the help of their colleagues at Bruker BioSpin. This pulse program (Figure 13) extends the work of Dvinskikh and Furó, applying their methods to model membrane systems. The pulse program used by Dvinskikh and Furó used the MREV8 sequence to prevent signal loss due to dipolar coupling in CaF_2 crystals. For this work, the MREV8 sequence prevented signal loss due to anisotropic effects in lipid-membrane systems during the position encoding and decoding time periods (δ), as well as during FID acquisition, in a PGSTE NMR pulse program. Given sufficient gradient strength, this should make observing signal attenuation due to diffusion possible. The pulse program shown in Figure 13 includes the line-narrowing sequence during δ and signal detection, and it is designed to measure diffusion in a sample using PGSTE NMR.

Our experimental work was divided into several phases, with our final goal being to capture an MREV8 enhanced spectrum of a model membrane system using MP-PGSTE NMR. The first experiments applied a simple pulse-and-detect program (Figure 4) that included the MREV8 sequence to DMPC MLVs and studied the effects of the various parameters on the observed

linewidths. The next set of experiments sought to apply our MP-PGSTE pulse program to ethylene glycol, in order to verify the ability of the program to measure diffusion accurately. This required first measuring the self-diffusion of ethylene glycol using a standard PGSTE NMR program, to provide a set of data for comparison. The final set of experiments were to apply the MP-PGSTE NMR pulse program to model-membrane systems, in hope of obtaining a spectrum. Given the strength of the gradients available in our lab, and the scale of confinement provided by the model-membrane systems discussed, it was not expected that our equipment would be able to measure the diffusion of lipids.

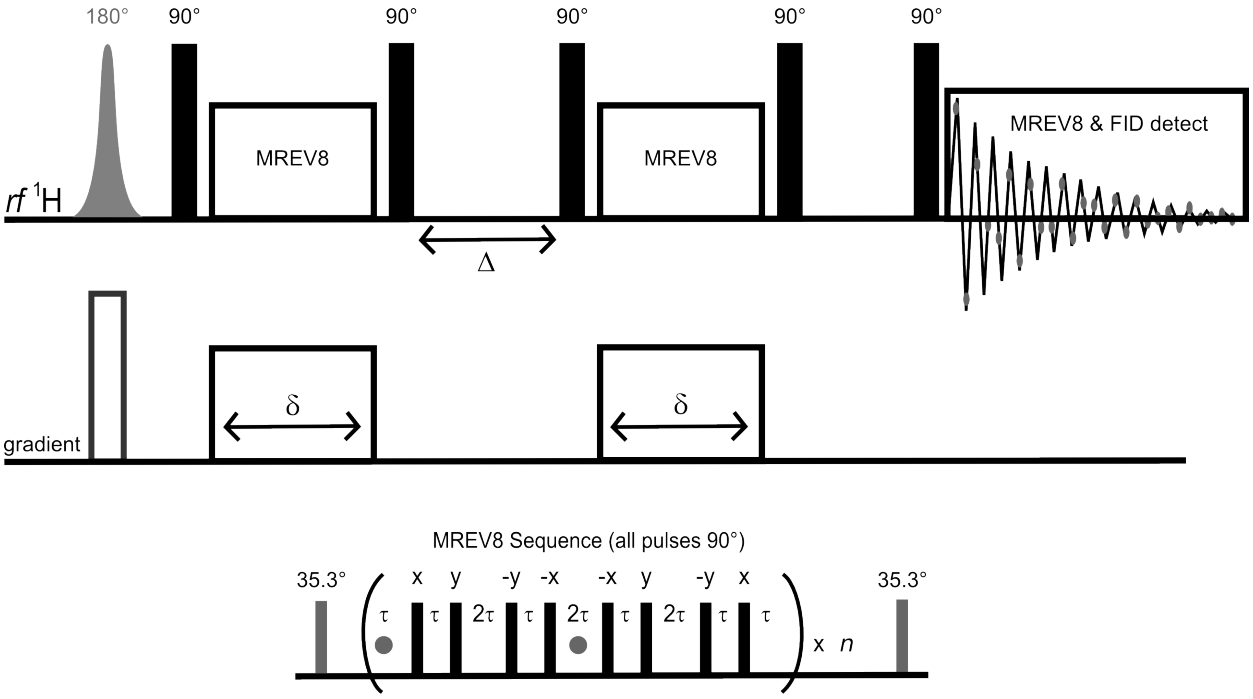

Figure 13: An MP-PGSTE NMR pulse program. The diagram shows the MP-PGSTE NMR pulse program that was constructed and used for the work presented. The program starts with a shaped 180° rf slice-selection pulse that includes a gradient pulse.* Use of the MREV8 sequence requires a preparatory pulse to orient the magnetization along the magic-angle; preparatory pulses are shown in gray and immediately follow (or precede) the 90° STE pulses. Two MREV8 blocks occur during the spatial encoding and decoding time, δ, while a third is used during FID acquisition.

*The MREV8 sequence, when applied, has an effective bandwidth within the NMR spectrum (determined by experimental parameters) where it homogeneously affects the sample, and the use of magnetic field gradients will broaden the bandwidth of the NMR signal. To ensure that the signal acquired is homogeneously affected by the MP sequence and to compensate for broadening due to the gradients, a slice-selection scheme is employed.

II. MATERIALS AND METHODS

Multilamellar vesicles (MLVs) of dimyristoylphosphatidylcholine (DMPC) were prepared by mixing 10 mg of DMPC in 50 μL of D_2O and heating the mixture in a 60ºC water bath for at least 2 hours. The sample mixture was then temperature cycled by moving it from the hot water bath to an ice bath, with 2 min of vortexing in between, and allowing the sample to stay in each bath for 20 min at a time. A minimum of 3 temperature cycles were applied to each sample. After the final time in the ice bath, the sample was transferred into a 4 mm x 10 mm cylindrical ZrO_2 rotor, using a spherical insert, with an internal volume of 50 μL.

Large unilamellar vesicles (LUVs) of DMPC were prepared by using a combination of extrusion followed by dialysis to obtain a sample of uniformly-sized LUVs, as published by Szostak and Zhu.[18] The size of the vesicles was measured via dynamic light scattering (DLS). The DMPC MLV size was also measured using MAS-NMR diffusion-imaging.

All NMR spectra were collected using Topspin 1.3 with a Bruker (Bruker Biospin, Billerica, MA) Avance AVI series spectrometer, BCU05 Variable Temperature Control Unit, and an 11.7 T magnet. Diffusion measurements were carried out using a Bruker 4mm gradient-equipped HXY MAS probe. Typical ^{1}H NMR 90° pulse lengths were 1.8 – 2.5 μs, at a power level of ~138 kHz. The self-diffusion of ethylene glycol (EG) was measured at 300 K via PGSTE ^{1}H NMR, with the sample rotor held static at 54.7°. The larger ethyl peak was observed and its attenuation was measured to determine the diffusion constant, using the methods described above.

III. RESULTS AND DISCUSSION

The MP NMR technique requires windowed acquisition, where data points are collected in between two high-powered *rf* pulses, as shown in Figure 4. These high-powered pulses present the risk of overloading the receiver if the detection gate is open while the *rf* coil is transmitting. Because the risk of damage is so great, windowed acquisition is not included in the Bruker-supplied pulse programs, and so we wrote a pulse program that had windowed acquisition explicitly included (Appendix A). The time required for each acquisition command to be executed was significant (~5 μs) to the time needed to execute the pulse sequence, creating a functional minimum for cycle time (~ 40 μs).

Most commercially available gradient-equipped solid-state NMR probes (including those used for this work) will arc if a pulse power higher than 178 kHz is used. When arcing occurs inside the probe, power is diverted away from the *rf* coil via the electrical arc, reducing the *rf* pulses' effects on the sample, and the arc can damage the electronics. This limitation meant that the τ value for the MREV8 sequence (Figure 4), and therefore the cycle time of the pulse sequence, had a lower limit of about 3.4 μs, corresponding to a cycle time of 40.8 μs, preventing our experiments from using shorter cycle times (the cycle time is 12τ).

The line-narrowing provided by the MREV8 pulse sequence proved to be especially sensitive to slight adjustment of experimental parameters, demanding exquisite precision to obtain the best results. In DMPC MLVs, a 0.05 μs change in the 90° *rf* pulse time in MREV8 altered the observed line widths (full-width at half-maximum, FWHM) by approximately 15-20 Hz (about a 10% change in FWHM). The dependence of linewidth on the pulse time is shown in Figure 14. In Figure 14, the width of the acyl-chain resonance is plotted versus the length of the 90° pulse

time. There are two distinct regions shown in Figure 14, from 1.45-1.65 μs, and from 1.65-1.90μs; the former region shows major changes in line-width with slight adjustment of the pulse time, while the latter shows comparatively less change in line-width as the pulse length changes.

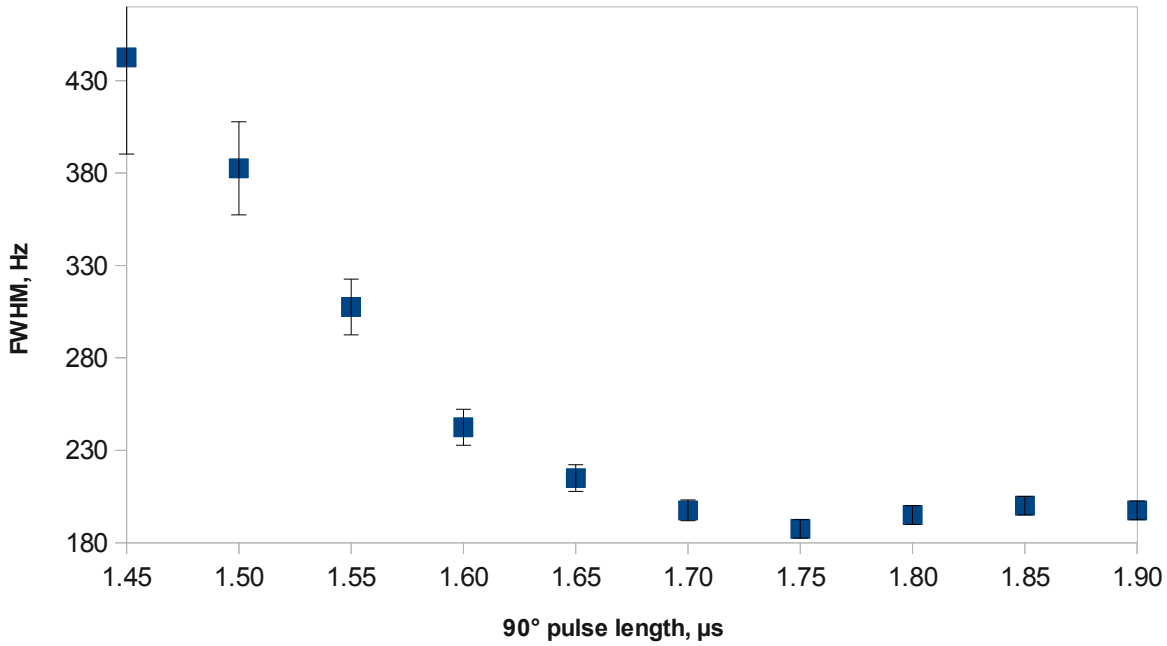

Figure 14: Sensitivity of DMPC acyl-chain linewidth to MREV pulse calibration. The plot reveals the optimum pulse length for the MREV8 sequence when applied to DMPC MLVs. The observed acyl-chain linewidth shows a strong sensitivity to the pulse time.

Similar to the 90° pulse time, the "magic angle" *rf* pulse length (the 35.3° pulse in Figure 4 that orients the magnetization to the magic angle) had a significant effect on the narrowing provided by the MREV8 sequence. This pulse orients the nuclear magnetization of the sample to the magic-angle relative to the -*z* axis, taking advantage of the dipole-dipole Hamiltonian given in Equation 1; the subsequent pulses then exploit the spin term as described earlier. The magic-angle pulse length must be accurately determined in order to optimize the line-narrowing provided by the MREV8 sequence. Changes on the order of 100 ns affected the line width observed when the MREV8 sequence was applied. Figure 15 shows a plot of the FWHM of the DMPC acyl-chain resonance versus the MREV8 preparatory pulse length. As the plot in Figure 15 shows, the dipole-dipole effects were modulated the most when the pulse length was between 0.65-0.71 μs.

The MREV8 sequence relies on the precise manipulation and choreography of the nuclear magnetization in the sample, in order to produce an NMR spectrum with reduced dipole-dipole effects. The *rf* pulse times, as well as the delay times in MREV8 sequence, affect the magnetization by causing it to evolve (Figure 4). The delay lengths were adjusted by holding the *rf* pulse times constant while changing the MREV8 cycle time. Changes to the cycle time affected the FWHM of the DMPC acyl-chain peaks, as shown in Figure 16. As expected from the literature,[10, 13-14] shorter cycle times increased the effectiveness of the pulse sequence, yielding smaller line widths. While these timing-related parameters affected the observed line width noticeably, the greatest effect on line-narrowing ability came from adjustment of the carrier frequency.

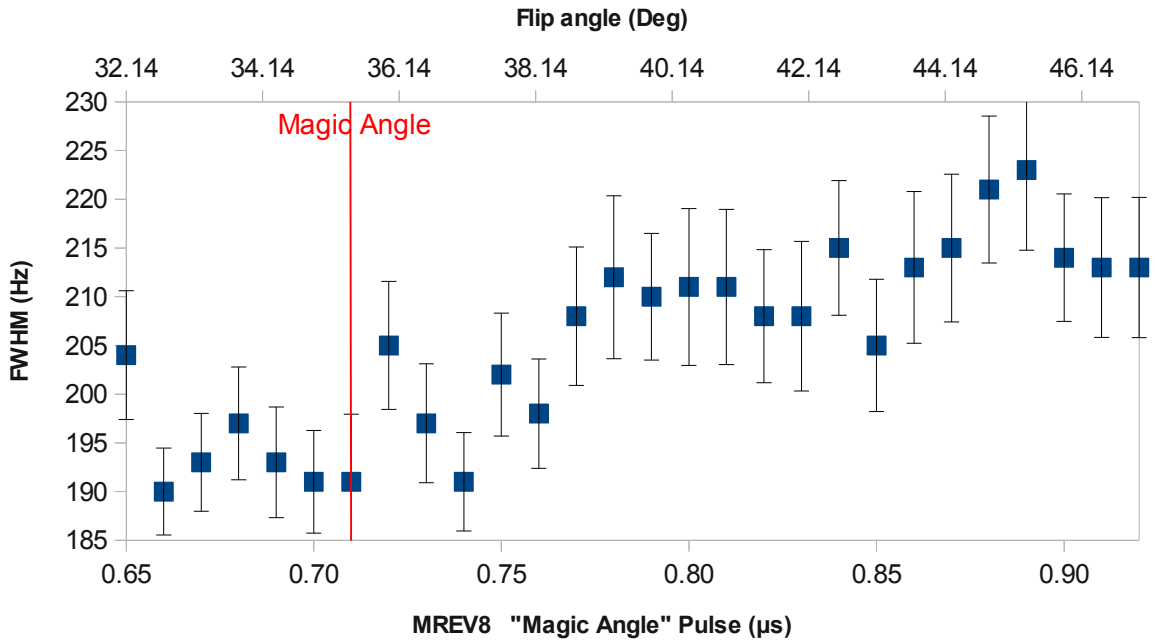

Figure 15: Linewidth weakly depends on "Magic Angle" pulse length. The plot shows how changes to the MREV8 preparatory pulse (the 35.3° pulse in Figure 4) affected the FWHM of the acyl-chain resonance in DMPC MLVs. The red line indicates the pulse length that has been calculated from a 90° pulse calibration.

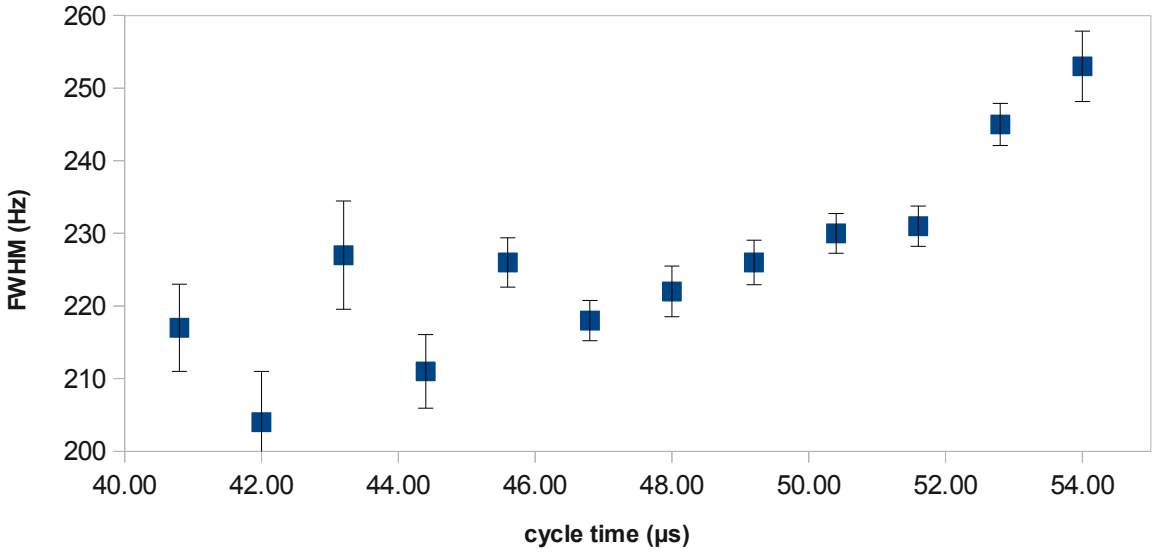

Figure 16: Shorter cycle times give reduced acyl-chain linewidths. The plot shows how the line width of the acyl-chain resonance of DMPC MLVs was affected by changes to the cycle time when the MREV8 sequence was applied.

When changed by as little as 50 Hz, the carrier frequency had a noticeable effect on the line-narrowing efficiency of the MREV8 sequence. For DMPC MLVs, setting the carrier frequency 2.5 kHz off-resonance from the acyl-chain peak yielded the best line width, 195 Hz, with a cycle time of 43.2 μs. This represented a $\tau^{4.1}$ dependence of line width on the pulse sequence timing, and was reasonably consistent with expectations. During analysis of ethylene glycol, setting the carrier frequency to 0.70 kHz off-resonance of the ethylene peak, the observed linewidth was approximately 95 Hz with a cycle time of 40.8 μs. Thus, the line width had a $\tau^{3.7}$ dependence, which was consistent with the expectations described in equation 17 as well as in the literature.[10]

When the MREV8 pulse sequence was applied to DMPC MLVs, using a simple pulse and detect program (Figure 4), the line-narrowing effects were immediately apparent. As shown in the spectra in Figure 17, when the sample was static the intensities of the choline and acyl-chain peaks were increased relative to the water signal. In the top spectrum in Figure 17, the choline and acyl-chain resonances of the DMPC are broadened so much by anisotropic interactions that their peaks are practically lost in the baseline of the spectrum, making it impossible to measure their width. However, in the bottom spectrum in Figure 17, the same two resonances are clearly visible, and their width can be quantified. If the same resolution can be achieved using our MP PGSTE-NMR pulse program, shown in Figure 12, then it should be possible to make a diffusion measurement on a static lipid membrane system.

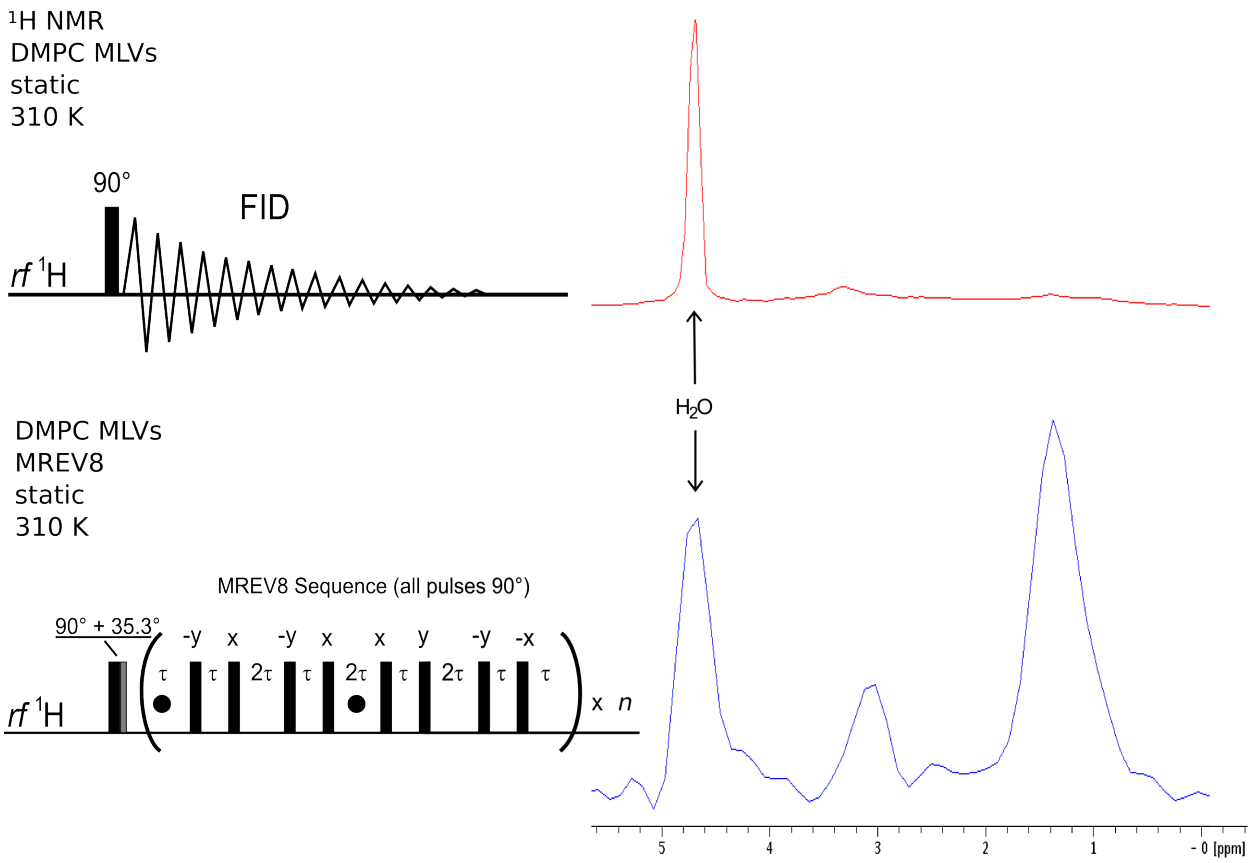

Figure 17: Applying MREV8 to DMPC Multi Lamellar Vesicles. The ^{1}H NMR spectra show the effects of the MREV8 sequence when applied to static DMPC MLVs. In the top spectrum, without MP-NMR, the water signal (4.70 ppm, FWHM = 60 HZ) is the dominant feature; in the bottom spectrum, using the MREV8 sequence, the choline (3.1 ppm, FWHM = 225 Hz) and acyl-chain (1.2 ppm, FWHM = 195 Hz) resonances are observed. Both spectra were collected at 310 K.

When using the MREV8 sequence, the applied trains of *rf* pulses cause a scaling of the chemical shift. This scaling is predicted by Rhim, Elleman, and Vaughan:[14]

$$s = \sqrt{2}(1+2a)/3 \qquad (27)$$

$$\text{with: } a = (3\tau_w/t_c)[(4/\pi)-1] \qquad (28)$$

where s is the scaling factor, τ_w is the 90° pulse time, and t_c is the cycle time of the pulse sequence. Using our typical pulse and cycle times, 1.85 μs and 42.00 μs respectively, Equation 27 predicts s = 0.505. The scaling factor can also be determined experimentally by comparing the known distance between two resonances in the presence and absence of the decoupling sequence. The ratio of those two distances provides a scaling factor which can be applied to the dwell time during acquisition. In this work, s was typically about 0.470, representing a 7% difference from the predicted value. This scaling factor, when determined and applied correctly, allowed direct comparison of spectra that used a decoupling sequence with those that did not.

Before applying our MP-PGSTE NMR pulse program to DMPC samples, it was necessary to evaluate its effects on a well known sample that does not exhibit anisotropic effects, in order to assess any artifacts that may be introduced by the program. For this task, we chose to use ethylene glycol (EG) due to its two distinct resonances as well as the temperature dependence of the chemical shift between those resonances. In order to establish a set of control data, the self-diffusion of EG was measured using a traditional PGSTE NMR pulse program (normally used in tandem with MAS, but here the sample was held static). As shown in Figure 18, the displacement of EG increased linearly with the allowed diffusion time, Δ, and EG was found to have a diffusion constant, D, of $6.5\,x\,10^{-11}\,m^2\,s^{-1}$. When compared to the literature, the percent difference was ~33% [Mitchell]. This difference may have resulted from using a static, rather than spinning sample, because the linewidth would have been larger in the static case. A larger linewidth would increase the uncertainty of the signal attenuation measurements necessary for determining displacement of EG. Greater linewidth also could have resulted from using an NMR

probe designed for solid-state rather than solution-state work. Furthermore, the low value obtained for the diffusion coefficient of EG could have resulted if the recorded temperature of the sample were not correct (perhaps due to some error with the temperature control unit). No matter what the case, the percent difference between the experimental and literature value of the diffusion constant of EG seems to indicate agreement to a reasonable degree and show great precision. In Figure 19, the initial results from the EG analysis by MP PGSE NMR were successful, although removing artifacts near the carrier frequency (~ -1.00 ppm) remains a challenge.

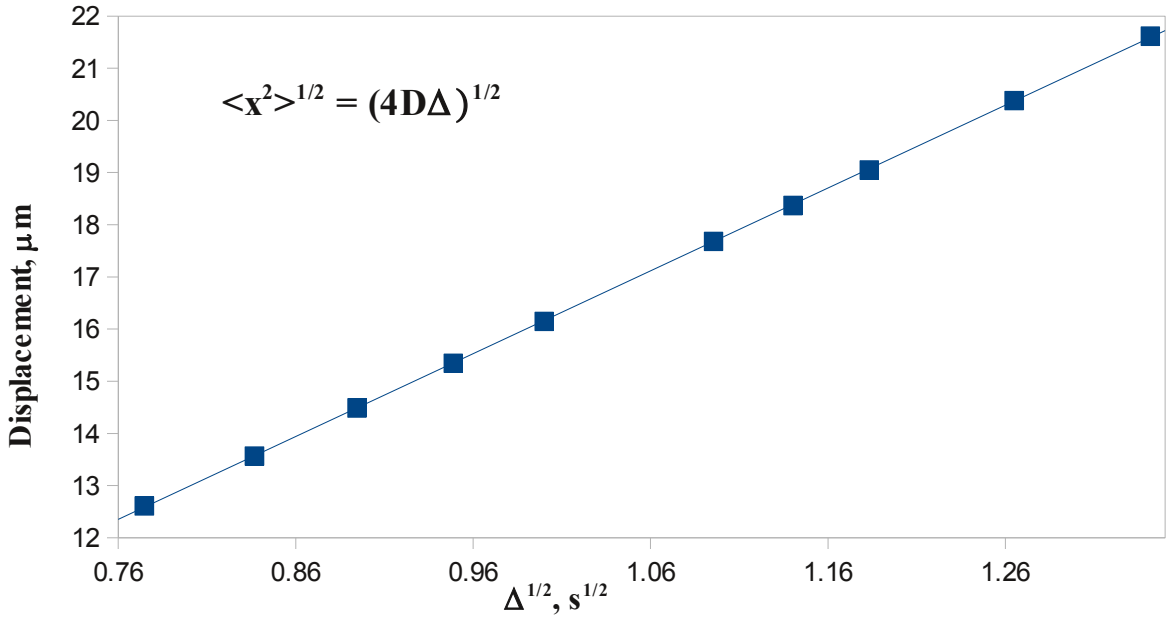

Figure 18: Ethylene Glycol shows free diffusion at 300 K.

A fit of displacement versus Δ1/2 for ethylene glycol (EG) shows a linear trend, as expected. The self-diffusion of EG was measured at 300K using a PGSTE pulse program with the sample held static. The self-diffusion coefficient was determined to be $6.5\,x\,10^{-11} m^2\,s^{-1}$, which is a 33% difference from the value reported at 298 K.[19]

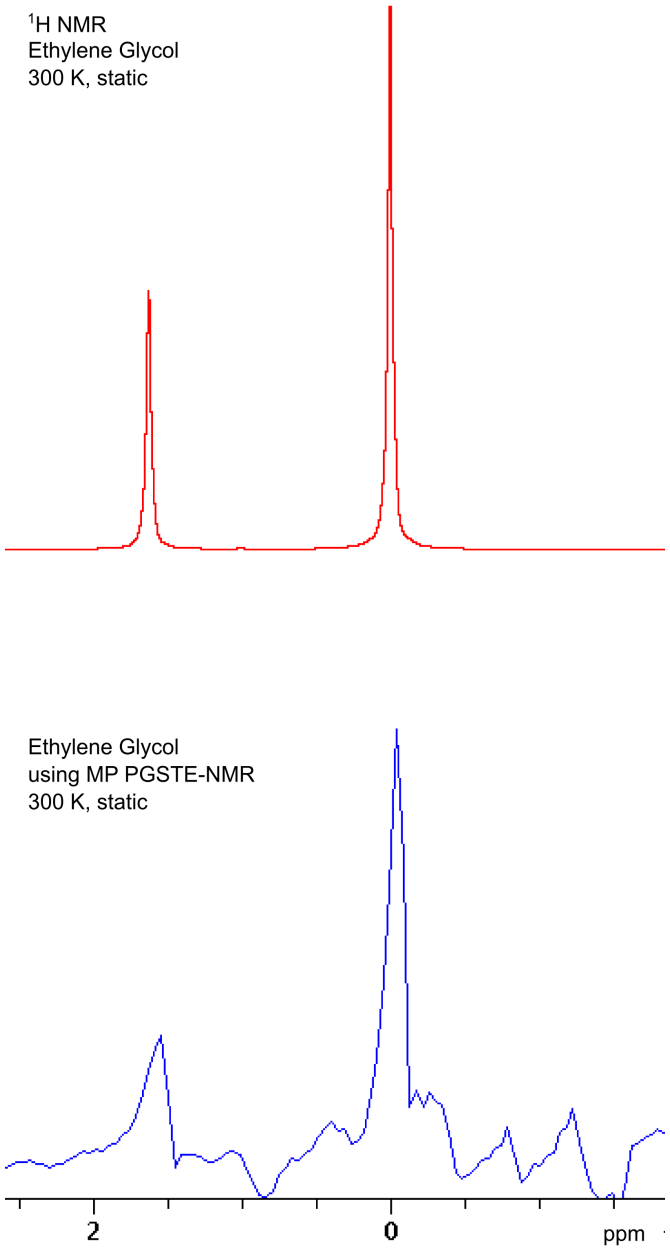

Figure 19: Applying MP PGSTE NMR to EG. ^{1}H NMR of ethylene glycol under normal and MP PGSTE NMR conditions. The upper spectrum shows resonances at 0.00 (FWHM ~ 16 Hz) and 1.63 ppm (FWHM ~18 Hz). The lower spectrum shows resonances at 0.00 ppm (FWHM ~60 Hz) and 1.63 (FWHM ~90 Hz). The broadening of the EG resonances is consistent with the use of pulsed-field gradients.

After seeing the results of the application of the MP-PGSTE to EG, further work was done to investigate whether the MREV8 sequence was causing any heating effects. The rapid succession of *rf* pulses applied during the encoding and decoding periods of our pulse program can lead to sample heating, and prior work done in this area compensated for this effect by extending the pre-scan delay to allow the heat to dissipate.[2] We were able to measure the heating caused by our pulse program by collecting spectra at increasing δ and measuring the distance (in ppm) between the EG resonances. Figure 20 shows a plot of two data sets, each collected using various pre-scan delays. The average temperature change when using a pre-scan delay of 30 s and δ range from 1500-7000 μs was approximately 2 K, which corresponds to a 0.02 ppm change in the distance between the two EG resonances. Because 2 degrees of temperature change may influence the state of lipids in a bilayer, future work must investigate methods to compensate for the heating effects caused by the use of MP NMR before our pulse program can be applied to biological samples.

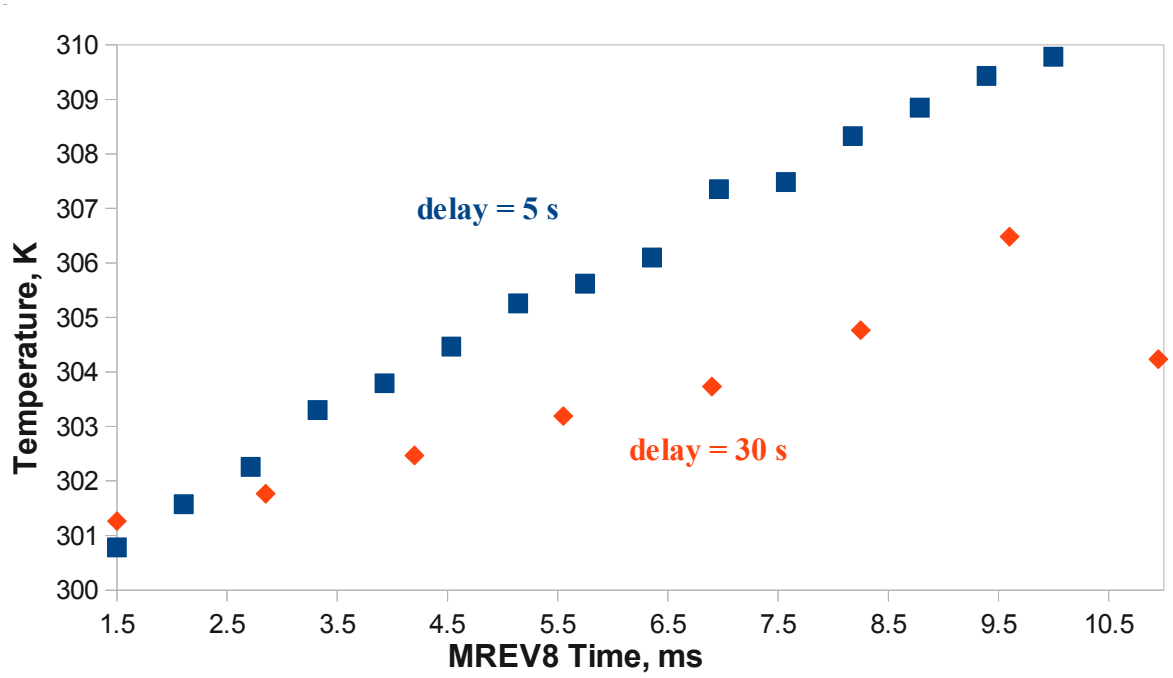

Figure 20: Heating effects caused by MREV8. The plot shows the rising temperature of ethylene glycol as the MREV8 sequence is applied as part of our MP PGSTE NMR program (Figure 10) for increasing amounts of time. The two data sets were collected using different pre-scan delays, with the longer delay decreasing the rate of heating only slightly.

This work has shown that MP NMR can indeed be useful for line-narrowing in lipid bilayer samples, and that this technique can be combined with PGSTE NMR for measuring the lateral diffusion of lipid molecules within a membrane. A MP-PGSTE NMR pulse program was constructed for use with a Bruker spectrometer, and it was successfully applied to measuring the self-diffusion of ethylene glycol. Future work should focus on application of the MP NMR technique to model membrane systems and biological samples. Successful application will require NMR hardware with stronger magnetic field gradients than were available for the work presented.

IV. REFERENCES

1. Crawford, S.M. e*t al.; J. Am. Chem. Soc.* (**1980**), 102 (11), 3728-3732.

2. Dvinskikh, S. V.; Furó, I., *J. Magn. Res.* (**2000**), 144 (1), 142-149.

3. Cho, H. S.; Dominick, J. L.; Spence, M. M.; *J. Phys. Chem. B.* (**2010**) 114, 9238-9245.

4. McIntosh, T. J., *Lipid Rafts*. Humana Press: Totowa, New Jersey, 2007.

5. Simons, K.; Ikonen, E. *Nature* (**1997**) 387, 569-572

6. Mañes, S.; del Real, G.; Martínez-A, C.; *Nat. Rev. Immunol.* (**2003**), 3, 557-568.

7. Kilby, J.M.; Eron, J. J.; *N Eng J Med* (**2003**), 348, 2228-38.

8. Levitt, M. H., *Spin Dynamics: Basics of Nuclear Magnetic Resonance*. John Wiley & Sons, Ltd: New York, 2001.

9. Callaghan, P. T., *Principles of Nuclear Magnetic Resonance Microscopy*. Oxford University Press: Oxford, 1991.

10. Garroway, A. N.; Mansfield, P.; Stalker, D. C. *Phys. Rev. B*. (**1975**), 11 (1), 121-138.

11. Duer, M. J. *Solid State NMR: Principles and Applications*. Blackwell Science: Oxford, 2002.

12. Burum, D. P.; Rhim, W. K.; *J. Chem. Phys*. (**1979**), 71 (2), 944-956.

13. Rhim, W. K.; Elleman, D. D.; Vaughn, R. W.; *J. Chem. Phys*. (**1973**), 58, 1772.

14. Rhim, W. K.; Elleman, D. D.; Vaughn, R. W.; *J. Chem. Phys*. (**1973**), 59, 3740.

15. Gawrisch, K.; Gaede, H. Measurement of Lateral Diffusion Rates in Membranes by Pulsed Magnetic Field Gradient, Magic Angle Spinning-Proton Nuclear Magnetic Resonance. In *Lipid Rafts*; Dopico, A. M., Ed.; Humana Press: Totowa, New Jersey, 2007.

16. Legget, J.; Crozier, S.; Blackband, S.; Beck, B.; Bowtell, R.W.; *Concept. Magnetic Res. B*. (**2003**), 168, 38-46.

17. Anderson, W.; *Rev. Scientific Instruments*. (**1961**), 32 (3), 241-250.

18. Zhu, T. F.; Szostak, J. W.; *PloS One*. (**2009**), 4 (4).

19. Chandrasekhara, N.; Krebsb, P.; *J. Chem. Phys*. (**2000**), 112 (13), 5910.

V. APPENDIX

```
;MREV8_STE_1D
;assembled from stegp1s1d v1.3.10.1, and mrev8.av1
;KB Univ. of Pitt.
;
;1D sequence for diffusion measurement using stim.-echo with square gradient pulses, mrev8
explicitly
;programmed during gradient pulses and acquisition
;
;$CLASS=HighRes
;$DIM=1D
;$TYPE=homonuclear decoupling
;$SUBTYPE=explicit acquisition

; THIS PULSE PROGRAM CAN BE USED IN ANALOG AND DIGITAL MODE
; ANALOG MODE IS RECOMMENDED
; IN CASE OF DIGITAL MODE TAKE INTO ACCOUNT THAT THE NUMBER OF PULSES
; ON THE PROBE IS MULTIPLIED BY DECIM, SO TD SHOULD BE REDUCED
ACCORDINGLY.
; ALSO: SETTING SW OR SWH MUST BE SELECTED SUCH THAT DECIM IS 2 OR
(MAXIMUM) 4
; WHICH MEANS THAT THE ACTUAL SWH GIVEN BY THE PULEPROGRAM TIMING
MUST BE
; ENTERED AS 1s SWH BEFORE TRANSFORM. RESETTING OF THE STATUS SW, SWH,
OR DW MAY MAKE
; THE GROUP DELAY COMPENSATION FAIL, IN DIGITAL MODE, THEREFORE, A
LARGE
; 1ST ORDER PHASE CORRECTION MAY BE NECESSARY

; ANY SETTING OF DIGMOD, DW, SW, SWH WILL CHANGE FW, RESET FW TO
MAXIMUM BEFORE MEASURING
; TO AVOID DEADTIME OF ANALOG FILTERS

;set:
;p1 to 1.4-2.2 usec depending on probe arcing limit
;p9 to 2.5-4.5 usec, depending on probe deadtime, usually:
; - for 200 and 300 MHz, CRAMPS probe required or use 4.5 usec
; - for 400, 500 MHz CP probes use 3-3.5 usec, 2.5-3 usec with CRAMPS probes
; - for 600 MHZ or higher CP probes use 2.6-3 usec
;logical observe channel: f1
;logical pulse channel: f2
;physical observe SGU: SGU1
;physical pulse SGU: SGU2
```

;set proper o2 value, make sure o1=o2
;digmod: analog (or digital)

;chemical shift scaling:
;
;in analog mode dw can be set to the proper value before measuring (reset fw as described above)
;set dw=realdwell to obtain PMLG scaled chemical shift axis
;for approximately true scaling set dw=scaleddwell, this value is calculated using a typical scale factor of 0.48
;for precise true scaling set dw=realdwell*(experimental scale factor)
;
;in digital mode dw (or sw or swh) must be set to have decim=2 or decim=4 before measuring
;(reset fw as described above)
;set 1s dw to realdwell or scaleddwell prior to FT, adjust 1st order phase correction as
;described above

;parameters:
;p1 : f2 channel - high power 90 pulse
;p2: f2 channel- selective inversion pulse
;p9 : small window size (pulse center to pulse center)
;p14 :High power pulse with a flip angle of 35.3 degrees- it follows a 90 pulse and sets the mag. at the MA
;pl1 : f2 channel - power level for pulses (default)
;pl2 : = 120 dB, not used

;cnst25 : phase correction for magic angle pulse (p14) in MREV8
;p25 : dummy pulse to show cnst25 in ased
;p26 : dummy pulse to show cnst26
;p27 : dummy pulse to show cnst27
;o1 : observe offset, must be =o2
;o2 : pulse offset, optimize for resolution
;digmod=analog (or digital, but analog is preferred)

;p30: gradient pulse (little delta)
;d1 : relaxation delay; 1-5 * T1
;d3: defines the small delay in mrev8 cycle, d3*12=cycle time
;d4: use to set duration of gradient pulse during sel inversion pulse
;d20: diffusion time (big DELTA)
;d21: delay for blanking gradient

```
;NS: 8 * n, total number of scans: NS * TD0
;DS: 16 * m


#include <Avancesolids.incl>
#include <Grad.incl>
#include <Delay.incl>

"d9=0.1u"               ;sampling window for analog averaged aquisition
"d3=p9"                         ;use p9 to set the window size, by this default delay units are us
"d6=p30"                ;defines the duration of the square gradient pulse (little delta)

define delay dead               ;set expected deadtime to average value
"dead=1.2u"
define delay small              ;small window, defined by d3, 2.5-4.5 usec depending
"small=p9-p1"                   ;on probe deadtime
define delay acq                ;large window with data sampling
"acq=(2.0*p9)-dead-p1-d9-0.2u"                  ;data sampling takes d9 + 0.1 usec, 0.1 usec are for
switching from receive to transmit mode
define delay large                      ;large window
"large=(2.0*p9)-p1"

define delay realdwell                  ;this is the true dwell time, i.e. time between two data points
"realdwell=(6.0*p9/2.0)*decim"
define delay scaleddwell        ;the is the effective dwell time. i.e. including a typical MREV8
chemical shift scaling
"scaleddwell=realdwell*0.48"

define loopcounter count        ;make sure td datapoints are sampled
"count=(td/2+1)*decim"
"p25=1u*cnst25"                         ;dummy pulse to show cnst25 in ased
;"p26=1u*cnst26"                        ;dummy pulse
;"p27=1u*cnst27"                        ;dummy pulse
define loopcounter counta       ;loops the mrev8 sequence throughout little delta
"counta=(d6-p9*6)/(p9*6)"


;AV I and AV II hardware: blktr# is transmitter blanking for f# logical channel
;blktr1 for f1 logical channel; blktr2 for f2 logical channel
"blktr2 = 0.7u"

"l0=1"

"DELTA=d20"
```

```
1 ze
2 30m
  if "l0 % 2 != 0"
{
  RESETPHASE                    ;reset reference phase
  10u reset:f1 reset:f2         ;synchronise pulse and detection RF
  1u REC_BLK                    ;blank the receiving path
  0.1u
  scaleddwell                   ;to show scaleddwell in ased
  ip6+cnst25                    ;adjust cnst25 for minimum center spike
  ip7+cnst25
  ip8+cnst25
  ip9+cnst25
  ip11+cnst25
  20u BLKGRAD                   ;guarantees the gradient is off before scan
  d1 pl1:f2                     ;prescan delay and preset f2 power level
  50u UNBLKGRAD                 ;prepare gradient for use
  10u gron2                     ;selective inversion gradient on
  p2:sp1:f1                     ;selective inversion pulse
  d4 groff                      ;defines length of gradient pulse during selective inversion pulse
  p1:f2 ph1                     ;1st STE 90 pulse
  p14:f2 ph6                    ;MA prep pulse for mrev
  large gron1                   ;gradient on (start little delta)
  p1:f2 ph10^                   ;start mrev loop during little delta
3 small
  p1:f2 ph10^
  large
  p1:f2 ph10^
  small
  p1:f2 ph10^
  large
  p1:f2 ph10^
  lo to 3 times counta
  small
  p1:f2 ph10^
  large
  p1:f2 ph10^
  small
  p1:f2 ph10^
  large groff                   ;turn off the gradient (end little delta)
  p14:f2 ph7
  p1:f2 ph2                     ;2nd STE 90 pulse
```

```
  DELTA1                ;diffusion time- set d20 to desired DELTA
  p1:f2 ph3             ;3rd STE 90 pulse
  p14:f2 ph8            ;MA prep pulse for mrev
  large gron1           ;gradient on (little delta)
  p1:f2 ph10^           ;start mrev loop during little delta
 4 small
  p1:f2 ph10^
  large
  p1:f2 ph10^
  small
  p1:f2 ph10^
  large
  p1:f2 ph10^
  lo to 4 times counta
  small
  p1:f2 ph10^
  large
  p1:f2 ph10^
  small
  p1:f2 ph10^
  large groff           ;turn off the gradient
  p14:f2 ph9
  p1:f2 ph4
  d21 BLKGRAD                   ;blank gradient
  STARTADC              ;prepare ADC for sampling
  RGP_ADC_ON                    ;open ADC gate
  p1:f2 ph5
  p14:f2 ph11
  dead                  ;avg probe deadtime
  acq REC_UNBLK         ;open receiver path
  sample                ;this is sample macro
  0.1u
  p1:f2 ph10^           ;first pulse of MREV8, increment phase list pointer
 5 small
  p1:f2 ph10^
  large
  p1:f2 ph10^
  small
  p1:f2 ph10^
  dead
  acq REC_UNBLK         ;unblank receiver for data
  sample                ;this is sample macro
  0.1u
  p1:f2 ph10^           ;start next MREV8 loop
```

```
  lo to 5 times count       ;make sure td points are sampled
  1m iu0
  rcyc=2                    ;next scan
}

  RESETPHASE                    ;reset reference phase
  10u reset:f1 reset:f2     ;synchronise pulse and detection RF
  ;STARTADC                 ;prepare adc for sampling, set reference frequency
  1u REC_BLK                    ;blank the receiving path
  0.1u
  scaleddwell               ;to show scaleddwell in ased
  ip6+cnst25                ;adjust cnst25 for minimum center spike
  ip7+cnst25
  ip8+cnst25
  ip9+cnst25
  ip11+cnst25
  20u BLKGRAD                   ;guarantees the gradient is off before scan
  d1 pl1:f2                 ;prescan delay and preset f2 power level
  50u UNBLKGRAD                 ;prepare gradient for use

  p1:f2 ph1                 ;1st STE 90 pulse
  p14:f2 ph6                ;MA prep pulse for mrev
  large gron1               ;gradient on (start little delta)
  p1:f2 ph10^               ;start mrev loop during little delta
 30 small
  p1:f2 ph10^
  large
  p1:f2 ph10^
  small
  p1:f2 ph10^
  large
  p1:f2 ph10^
  lo to 30 times counta
  small
  p1:f2 ph10^
  large
  p1:f2 ph10^
  small
  p1:f2 ph10^
  large groff               ;turn off the gradient (end little delta)
  p14:f2 ph7
  p1:f2 ph2                 ;2nd STE 90 pulse
  DELTA1                    ;diffusion time- set d20 to desired DELTA
  p1:f2 ph3                 ;3rd STE 90 pulse
```

```
  p14:f2 ph8                ;MA prep pulse for mrev
  large gron1               ;gradient on (little delta)
  p1:f2 ph10^               ;start mrev loop during little delta
 40 small
  p1:f2 ph10^
  large
  p1:f2 ph10^
  small
  p1:f2 ph10^
  large
  p1:f2 ph10^
  lo to 40 times counta
  small
  p1:f2 ph10^
  large
  p1:f2 ph10^
  small
  p1:f2 ph10^
  large groff               ;turn off the gradient
  p14:f2 ph9
  p1:f2 ph4
  d21 BLKGRAD                       ;blank gradient
  STARTADC                  ;prepare ADC for sampling
  RGP_ADC_ON                        ;open ADC gate
  p1:f2 ph5
  p14:f2 ph11
  dead                      ;avg probe deadtime
  acq REC_UNBLK             ;open receiver path
  sample                    ;this is sample macro
  0.1u
  p1:f2 ph10^               ;first pulse of MREV8, increment phase list pointer
 50 small
  p1:f2 ph10^
  large
  p1:f2 ph10^
  small
  p1:f2 ph10^
  dead
  acq REC_UNBLK             ;unblank receiver for data
  sample                    ;this is sample macro
  0.1u
  p1:f2 ph10^               ;start next MREV8 loop
  lo to 50 times count      ;make sure td points are sampled
  1m iu0
```

```
  rcyc=2                        ;next scan
6 100m wr #0                    ;save data

exit

ph0=0
ph1= 0 2
ph2= 0 0 1 1 2 2 3 3
ph3= 0 0 1 1 2 2 3 3
ph4= 0 0 0 0 0 0 0 0 2 2 2 2 2 2 2 2
ph5= 0 0 0 0 0 0 0 0 2 2 2 2 2 2 2 2
ph6=(360) 270 ;270 0 90 180 ;the phase is set as (360/360 + number in degrees)
ph7=(360) 90 ;180 270 0
ph8=(360) 270 ;270 0 90 180
ph9=(360) 90 ;90 180 270 0
ph11=(360) 270 ;270 0 90 180
ph10=0 1 3 2 2 1 3 0
ph30=0
ph31=0 2 2 0 0 2 2 0

;for z-only gradients:
;gpz6: 1-100%


;use AU-program dosy to calculate gradient-file Difframp




;31303131313737352053656d706572204669
```